ADVANCED ELECTROMAGNETIC METHODS FOR AEROSPACE VEHICLES

Semiannual Progress Report
(July 1 - December 31, 1991)

by
Constantine A. Balanis
El-Budawy El-Sharawy
Shahrokh Hashemi-Yeganeh
James T. Aberle
Craig R. Birtcher

Telecommunications Research Center
College of Engineering and Applied Sciences
Arizona State University
Tempe, AZ 85287-7206

Sponsored by
Grant No. NAG-1-1082
National Aeronautics and Space Administration
Langley Research Center
Hampton, VA 23665

Contents

I. INTRODUCTION

The Advanced Helicopter Electromagnetics (AHE)-Industrial Associates Program continues its research activities centered on issues that advance technology related to helicopter electromagnetics. The topics of research have been identified and supported by the members of the program. The Advisory Task Force of the AHE program reviews the topics of research and recommends areas of research interest to the group.

This progress report has focused on the following three major topics:

1. Composite Materials
2. Precipitation Static - Corona Discharge
3. Antenna Technology

In Composite Materials the research has focused on the measurements of the electrical properties of composite materials, and the modeling of material discontinuities and their effect on the radiation pattern of antennas mounted on or near material surfaces. Samples of the materials were provided by Sikorsky Aircraft and AVRADA (through SRI). Measurements of the electrical properties of these materials at microwave frequencies have already been made, and they have been reported in previous progress reports. These properties have been used to model antenna performance when mounted on composite materials. Since helicopter platforms include several antenna systems at VHF and UHF bands, measuring techniques are being explored that can be used to measure the properties at these frequency bands. Techniques are being developed to account for the presence of materials on the performance of the radiation characteristics of helicopter antennas. In particular, emphasis is placed on the representation and validity of the Green's function analysis. Separate computer codes have been developed which calculate the complex surface impedance of a finite size dielectric or composite material mounted on a perfect electric conductor (PEC). The imaginary part of the surface impedance accounts for radiation by the discontinuity. The impedance is computed using convolution theory and Green's function techniques. FFT techniques are used to evaluate integrals included in the convolution process.

During the second year of the AHE program the effort on corona discharge and precipitation static has been directed toward the development of a new two-dimensional Voltage Finite-Difference Time-Domain computer program. Results based on the simplified two-dimensional Voltage Finite-Difference Time-Domain program indicate the feasibility of utilizing potentials for simulating electromagnetic problems in the cases where potentials become primary sources. For example, the program can successfully predict the propagation constants for the longitudinal wave along a microstrip structure. In addition, efforts have been made to include the corona discharge mechanism into the two-dimensional Voltage FD-TD for a two-wire high voltage transmission line. Such a modeling is essential in understanding the discharge process and ultimately corona discharge mechanism by the sharp edge of an aircraft or helicopter structure.

In Antenna Technology the focus has been on Polarization Diverse Conformal Microstrip Antennas, Cavity-Backed Slot Antennas, and Varactor-Tuned Circular Patch Antennas. Through the AHE program, numerical codes have been developed for the analysis of two-probe-fed rectangular and circular microstrip patch antennas fed by resistive and reactive power divider networks. These codes can be used to evaluate the overall performance of polarization diverse conformal antennas in terms of return loss, axial ratio, cross-polarization level or polarization mismatch. In addition investigation has been initiated of slot antennas backed by cavities that are partially filled with ferrite. Experiments to measure the radiation pattern and efficiency of a prototype cavity-backed slot antenna have been performed at microwave frequencies. There is considerable interest in using this type of an antennas at VHF and UHF frequencies. Computer codes are currently under development to predict the performance of these antennas. These codes utilize rigorous, fully electromagnetic approaches and should provide us with a good deal of insight on how to design these antennas for optimum performance. The narrow bandwidth of conventional microstrip antennas can be overcome by using a varactor diode to vary its resonant frequency over a fairly wide bandwidth. By varying the voltage across the varactor, the capacitance of the equivalent antenna circuit and thus the resonant frequency of the antenna can be changed. The investigation of this type of an antenna has been started, and it will continue in 1992.

A detailed review of the progress of all of these topics is outlined in this report. Additional information of the progress of the AHE program during

1991 can be found in the previous semiannual progress reports.

II. COMPOSITE MATERIALS

A. Introduction

Nonmetallic material are now routinely an integral part of an airframe. However the introduction of such materials to the structure plays a key role on the performance of the on-board avionics and significantly increases the analytical complexity of the prediction problem.

In this section, theory and measurements of antennas on composite materials are presented and compared. Two different types of composite materials are discussed:

1. Materials of high conductivity, such as graphite epoxy and fiberglass with aluminum screens near the surface.

2. Materials of low conductivity, such as fiberglass and microwave absorbers.

Measurements of material properties for both types of material have been performed in our laboratory and presented in our previous progress reports. The results of these measurements are used to evaluate the surface impedance of the material. This surface impedance is used to model the composite material structure as wire-grid and the NEC code is used to model and predict the radiation patterns of monopole antennas on or near surfaces of composite material.

B. Modeling and Measurements of Antennas on High Conductivity Composite Materials

In this section, we first measure the properties of some high conductivity composite materials. Using the experimental data, we numerically predicted the effects of the materials on antenna patterns. The computed results finally compared with measurements.

1. Measurements of material properties

Three material samples provided by Sikorsky Aircraft, one fiberglass impregnated with graphite epoxy, one fiberglass with one aluminum screen on the

surface and one fiberglass with two aluminum screens embedded near one of the surfaces, were tested. Figure 1 shows the geometry and orientation of all three different material samples. All these samples are symmetric in the 0° and 90° orientations, whereas some anisotropy may exist in the 45° orientation. To measure the properties of the material in the 45° orientation, other samples have to be cut so that the electric field in the waveguide is parallel to the required orientation. This explains why a single waveguide mode, with a well known field orientation, has to be used to measure anisotropic materials. In addition, another fiberglass sample with one aluminum screen on the surface, made available through SRI (Stanford Research Institute), was examined.

The surface conductivity versus frequency of the graphite sample is shown in Figure 2 for two different orientations, 0° and 45°. As mentioned above, the structure is symmetric with respect to 0° and 90° orientations, as well as with respect to the 45° and 135° orientations. As shown in Figure 2, the conductivity of graphite epoxy is about 1000-1500 S/m in the 45° orientation and about 500-1000 S/m in the 0° orientation. The conductivity increases with frequency which makes this material a good choice for shielding against surges due to antenna switching, corona, discharge, etc., where the frequency spectrum of these transients spreads over a very broad range.

Figure 3a shows the conductivity measurements of the Sikorsky Aircraft fiberglass sample with one aluminum screen on the surface. The conductivity is almost isotropic and increases with frequency. The value of conductivity is less than that of the graphite sample (almost one third). Figure 3b shows the conductivity measured from the opposite side of the aluminum screen (dielectric side). The equivalent conductivity in this case is significantly reduced (by a factor of about 30 less than the front screen conductivity). This shows the necessity of placing the conducting screen near the outer surface of the helicopter to get good grounding effects. Similarly, the measured conductivities the SRI sample are shown in Figure 4.

Figures 5a and 5b show the effective conductivity of both sides of the fiberglass sample with two aluminum screens embedded near one of the surfaces. First, by embedding the screens inside the material, the conductivity, similar to the graphite material, became anisotropic. However, contrary to the graphite, the 0° orientation of this material has higher conductivity. The conductivity decreases with frequency which does not provide as good of a shielding against transients. The dielectric side has the lower conductivity,

as expected.

Conclusions and recommendations stemming from the above measurements include the possibility of adding aluminum screens to graphite materials to neutralize their anisotropy, if this is of significance. Also, keeping the aluminum screens at the surface, instead of embedding them inside the material, can be useful in avoiding reduction of the conductivity versus frequency.

2. Material effects on antenna patterns

The measured data of the high conductivity materials are used to predict their effects on antenna patterns. The surface impedance used in the computations can be expressed in terms of the conductivity as

$$Z_s = \sqrt{\frac{j\omega\mu_0}{\sigma}} \tag{1}$$

This impedance is used as a load to the segments in a wire grid, representing a composite material surface, used in the computation of the NEC code.

First, the radar cross section (RCS) of a square sample of graphite epoxy was computed and compared with measurements made in the EMAC facility at Arizona State University. The surface of the graphite was modeled as a wire grid with surface impedance given by Equation 1.

The graphite sample has dimensions of $1.5\lambda \times 1.5\lambda$ at 6 GHz. Initially, the grid mesh was chosen to be square (Figure 6a). As mentioned above, the conductivity of this material is anisotropic. To account for this anisotropy, a denser mesh (as shown in Figure 6b) is used to model the graphite surface by assigning different surface impedance to wires in different orientations. Wires in the 45° orientation are assumed to have lower surface impedance than wires in the 0° orientation. To save CPU time, the thickness of the sample (0.111 inches corresponding to 0.0564λ at 6 GHz) was neglected and the sample was assumed to be infinitely thin. Figures 7 - 10 show predicted and measured monostatic RCS patterns for two different azimuth angles and two different polarizations (soft and hard polarizations). The predictions include results obtained from the square mesh and the denser mesh discussed above, and for the sake of comparison, results obtained by modeling the graphite as perfect electric conductor (PEC). Good agreement has been obtained in all cases with the highest discrepancy of about 2 dB in the endfire direction,

probably due to neglecting the thickness of the sample. Using the measured value of graphite conductivity, instead of assuming it to be a perfect electric conductor, resulted in a better agreement with measurements in the endfire direction but gave very similar results to the PEC model in the broadside direction.

Second, at 6 GHz, radiation patterns of a gold plated $\lambda/4$ monopole on a graphite sheet of dimensions $1.5\lambda \times 1.5\lambda$ were computed, using the surface impedance given by equation Equation 1 where the conductivity was from the previous measurements. We also measured the radiation patterns at our facility as comparisons.

The structure under investigation is shown in Figure 11. The monopole was placed at the center of the sheet. A coaxial connector was used to connect the antenna to the test equipment. The thickness of the sheet was 0.111 in (0.0564λ at 6 GHz). The modeling of the graphite ground plane is identical to those used in the prediction of the RCS of this graphite sheet. The monopole was modeled as an infinitely thin PEC ($Z_s = 0$) wire. We anticipated that the coaxial connector in the back of antenna will have a minimal effect on the main beam of the antenna, therefore the connector was not modeled. The computed and measured results are plotted in Figures 12 and 13 for two different azimuth angles. Good agreement was observed between theory and measurements, except for the back portion of the pattern. This may be due to the absence of modeling of the coaxial connector and the test cable in the back of the antenna. Neglecting the thickness of the graphite sheet also may have contributed to some of the discrepancies near and at endfire directions. The agreement between predicted results based on the actual surface impedance of the graphite was somewhat better than that assuming the graphite to be a PEC.

Finally, we built another $\lambda/4$ monopole antenna on a SRI fiberglass substrate covered with aluminum screen on the antenna side. The dimension of the ground plane is 2λ x 2λ and the operating frequency is 4 GHz (the low end frequency of our ElectroMagnetic Antenna Chamber).

Based on its measured conductivity ($\sigma = 300\ S$), the surface impedance of this material was evaluated, using Equation 1, to be $Z_s = 5 + j5\ \Omega$. The antenna structure, similar to Figure 11 except that the ground plane is replaced with a fiberglass with aluminum screen facing up, was modeled by a single layer of wire grids, represent the aluminum screen, and the monopole antenna. The grid mesh was chosen to be square and the length of each wire

was 0.1λ. Figure 14 shows the measured and computed radiation patterns. Good agreement between theory and measurements is indicated except in the back region. This may be attributed to the fact that the fiberglass at the back of the antenna, the coaxial connector and test cable were not included in the model.

From the above examples, we believe that the NEC code can predict accurately high conducting material discontinuities. However, with the extensive use of nonconductive material in modern helicopter platforms, it is necessary to examine the capability of the NEC code in handling low conductivity or nonconductive materials.

C. Predicting and Measuring Effects of Low Conductivity Composite Materials on Antenna Patterns

In the first year of this work, we developed a solution for dielectric coated surfaces. This solution was validated only for very large surfaces. The accuracy of this solution degrades as the dimensions of the dielectric surface decreases. Furthermore, the analysis was not successful in predicting the impact of composite materials on the antenna efficiency (refer to our previous annual report on the radiation patterns of $\lambda/4$ monopole on a 2λ x 2λ partially-coated surface). Later on, we initiated an attempt to use a Green's function analysis for dielectric discontinuities using equivalent source techniques. With this technique, the effect of the discontinuity is introduced by a source of electric or magnetic fields to represent the difference in the fields with or without the dielectric coating. We explored two different approaches; the spectral domain and the spatial domain. We found the spatial domain to be difficult to apply to more than one discontinuity or to use for composite materials.

In our previous reports, we presented an iterative technique to calculate the surface impedance of a perfect conductor partially coated with a composite material. We found that this iterative technique will be extremely slow and computationally inefficient. So, we worked on the derivation of a closed form solution for the surface impedance of a partially covered perfect electrically conductor. We also extended this expression to include magnetic materials and material losses. For a partially covered perfect electric conductor as shown in Figure 15, the effect of discontinuity can be modeled, as

mentioned above, by a fully covered ground plane and equivalent sources. Using convolution theory, it is possible to prove that the surface impedance Z_s as a function of coordinates can be expressed as:

$$\overline{\overline{Z}}_s(x_0,y_0,t) = \left[\tilde{\overline{\overline{Z}}}_T(-\beta_x,-\beta_y,t) + \frac{j}{2\pi}\int_{-\infty}^{\infty} e^{jk_x x_0} sin(k_x w_x) \right.$$

$$\int_0^t \begin{pmatrix} 4\pi(\epsilon_r-1)\tilde{\overline{\overline{T}}}_E(k_x-\beta_x,-\beta_y,t-z) \times \hat{x}.\tilde{\overline{\overline{Z}}}_T(k_x-\beta_x,-\beta_y,z)\,dz\,dk_x \\ 4\pi(\mu_r-1)\tilde{\overline{\overline{Z}}}_T(k_x-\beta_x,-\beta_y,t-z) \times \hat{y}.\tilde{\overline{\overline{T}}}_J(k_x-\beta_x,-\beta_y,z)\,dz\,dk_x \end{pmatrix}$$

$$+\frac{j}{2\pi}\int_{-\infty}^{\infty} e^{jk_y y_0} sin(k_y w_y)$$

$$\left. \int_0^t \begin{pmatrix} 4\pi(\epsilon_r-1)\tilde{\overline{\overline{T}}}_E(-\beta_x,k_y-\beta_y,t-z) \times \hat{y}.\tilde{\overline{\overline{Z}}}_T(-\beta_x,k_y-\beta_y,z)\,dz\,dk_y \\ 4\pi(\mu_r-1)\tilde{\overline{\overline{Z}}}_T(-\beta_x,k_y-\beta_y,t-z) \times \hat{x}.\tilde{\overline{\overline{T}}}_J(-\beta_x,k_y-\beta_y,z)\,dz\,dk_y \end{pmatrix} \right]$$

$$\times \left[\tilde{\overline{\overline{T}}}_J(-\beta_x,-\beta_y,t) + \frac{j}{2\pi}\int_{-\infty}^{\infty} e^{jk_x x_0} sin(k_x w_x) \right.$$

$$\int_0^t \begin{pmatrix} 4\pi(\epsilon_r-1)\tilde{\overline{\overline{Y}}}_T(k_x-\beta_x,-\beta_y,t-z) \times \hat{x}.\tilde{\overline{\overline{Z}}}_T(k_x-\beta_x,-\beta_y,z)\,dz\,dk_x \\ 4\pi(\mu_r-1)\tilde{\overline{\overline{T}}}_J(k_x-\beta_x,-\beta_y,t-z) \times \hat{y}.\tilde{\overline{\overline{T}}}_J(k_x-\beta_x,-\beta_y,z)\,dz\,dk_x \end{pmatrix}$$

$$+\frac{j}{2\pi}\int_{-\infty}^{\infty} e^{jk_y y_0} sin(k_y w_y)$$

$$\left. \int_0^t \begin{pmatrix} 4\pi(\epsilon_r-1)\tilde{\overline{\overline{Y}}}_T(-\beta_x,k_y-\beta_y,t-z) \times \hat{y}.\tilde{\overline{\overline{Z}}}_T(-\beta_x,k_y-\beta_y,z)\,dz\,dk_y \\ 4\pi(\mu_r-1)\tilde{\overline{\overline{T}}}_J(-\beta_x,k_y-\beta_y,t-z) \times \hat{y}.\tilde{\overline{\overline{T}}}_J(-\beta_x,k_y-\beta_y,z)\,dz\,dk_y \end{pmatrix} \right]^{-1} \tag{2}$$

where

$$\beta_x = k_0 sin(\theta)cos(\phi) \tag{3}$$

$$\beta_y = k_0 sin(\theta)sin(\phi) \tag{4}$$

and $\overline{\overline{Z}}_T, \overline{\overline{Y}}_T, \overline{\overline{T}}_E, \overline{\overline{T}}_J$ are the transmission matrices of the composite material.

It is clear from the above equation that the value of the surface impedance depends on the incidence angle θ as shown in Figure 11. This makes it necessary to run the NEC code for different angles. We wrote a computer

program to calculate the surface impedance for different values of θ and ϕ (azimuthal angle). At the present time this code uses regular inverse Fourier transforms to calculate Z_s. We plan to use IFFT in the future to save CPU time.

To verify our theory, we built a $\lambda/4$ monopole antenna at 10 GHz on a 2λ x 2λ ground plane. The ground plane was partially covered with a lossy material of $\epsilon_r = 10 - j3.8$ and $\mu_r = 2.12 - j1.5$, as shown in Figure 16. In our computations, three values of the surface impedance at $\theta = 15°, 45°$ and 75° were used. The computed versus measured radiation pattern are shown in Figure 17. The calculated radiation pattern for the antenna on a perfect electric conductor (without the lossy material) is also displayed. The effect of the lossy material is to reduce antenna efficiency. The calculated pattern using our new theory was somewhat higher (by about 4 dB in the main lobe) than the measured value. The reasons for this discrepancy may be:

1. Material properties are not known accurately. We plan to build another antenna on a material with well known properties, such as Teflon or Duroid.

2. More values of the surface impedance at different angles are required. This will require running the NEC code several time and is expected to consume a lot of CPU time.

D. Conclusions

This section presented measurements and predictions of composite materials on antenna patterns. Two categories of composite materials were examined.

The first type are materials of high conductivities, including graphite epoxy and fiberglass with an aluminum screens. Their conductivities were measured and then used in pattern computations with the NEC code. The predicted results showed good agreements with measurements. Thus, we conclude that the surface impedance given by Equation 1 can be used, as loads in the NEC wire grid model, to successfully predict the effects of the structure discontinuity if the composite materials have high conductivities.

The second type are materials with low conductivities, such as microwave absorbers. We developed computer codes to calculate the complex surface impedance of a finite size dielectric or low conductivity composite material.

We built and tested a monopole antenna on a partially covered ground plane. Although predictions of the radiation pattern of such an antenna show the same trend as the measured pattern, the computed pattern was higher than the measured pattern.

E. Future Work

Including the effects of material discontinuities on the radiation patterns of antennas is a most challenging problem. Our efforts so far have shown that it is possible to include these material discontinuities in our analytical models. However, there are a number of issues need to be addressed. First, the code has to be validated by carrying out further radiation pattern measurements and computing the complex surface impedance for many values of the incidence angle (we used only three angles in the above theoretical work). The theory will also be used to study the scattering from simple structures such as plates and cubes. We have plans to further improve the accuracy and the computational efficiency of our code by implementing IFFT techniques in our calculations. Finally, complex structures, such as helicopters and other complicated platforms will be investigated.

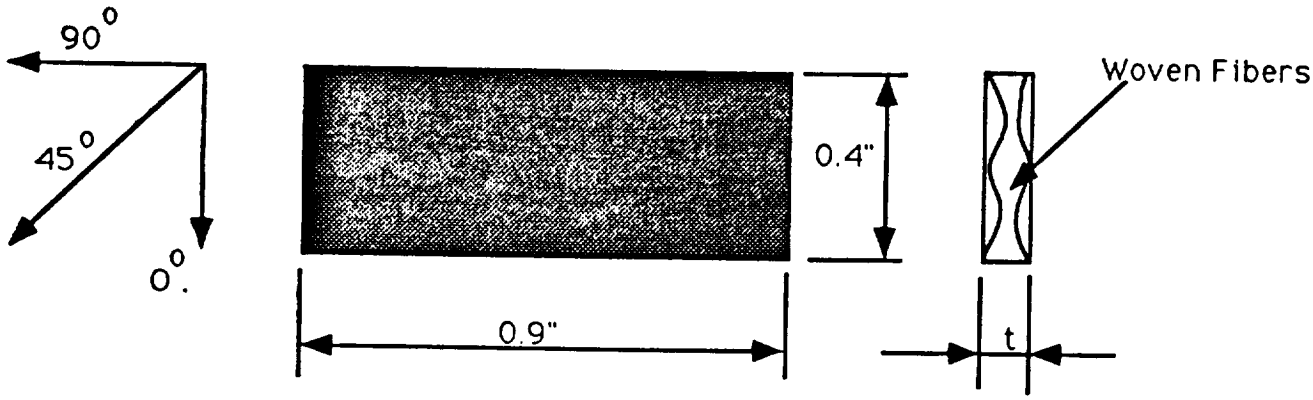

t= 0.111 in for graphite
t= 0.058 in for fiberglass with one screen
t= 0.062 in for fiberglass with two screens

Figure 1: Geometry of the composite material samples.

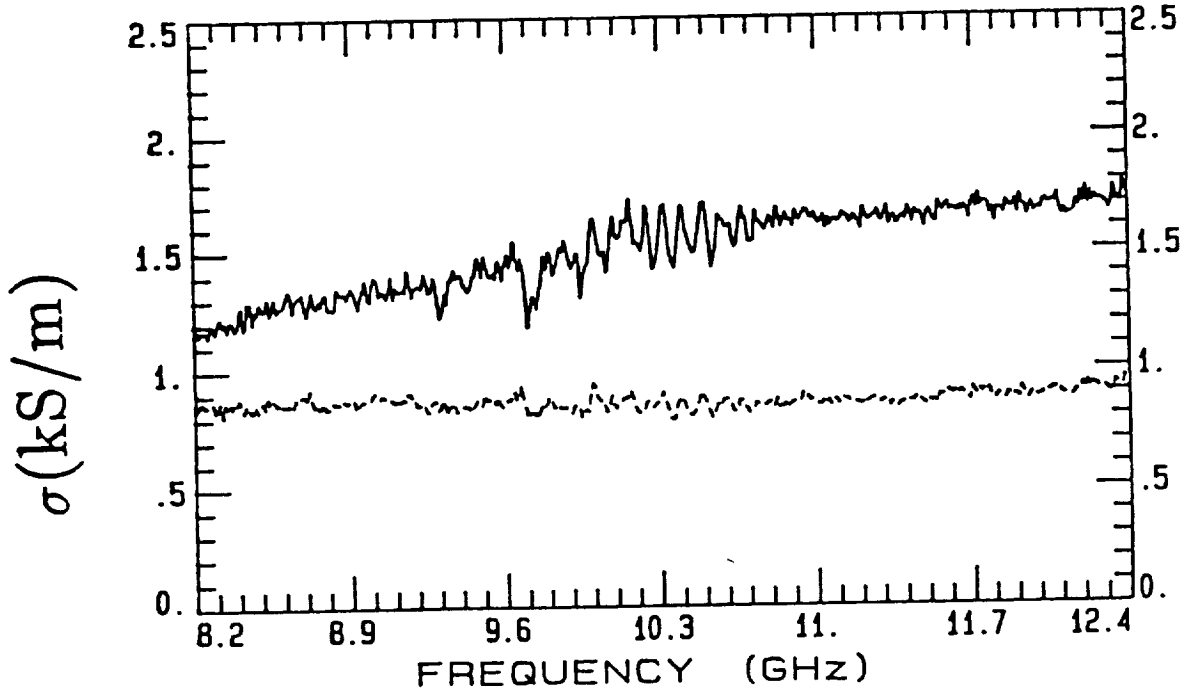

Figure 2: Conductivity of the graphite in kS/m.

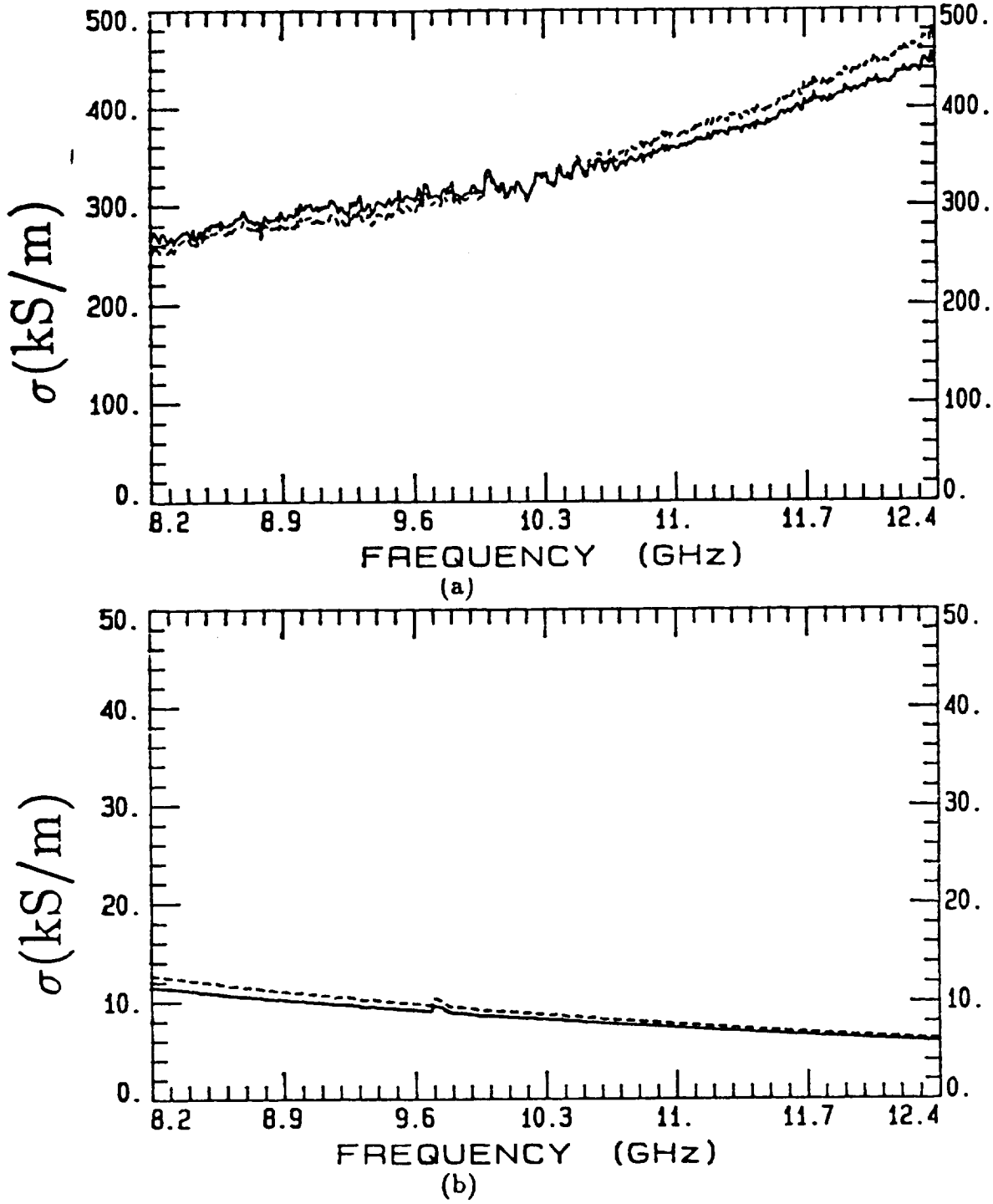

Figure 3: Conductivity of the Sikorsky fiberglass with one Aluminum screen, where Solid line: 45°; Dotted line: 0°. **a.** Screen side, **b.** Dielectric side.

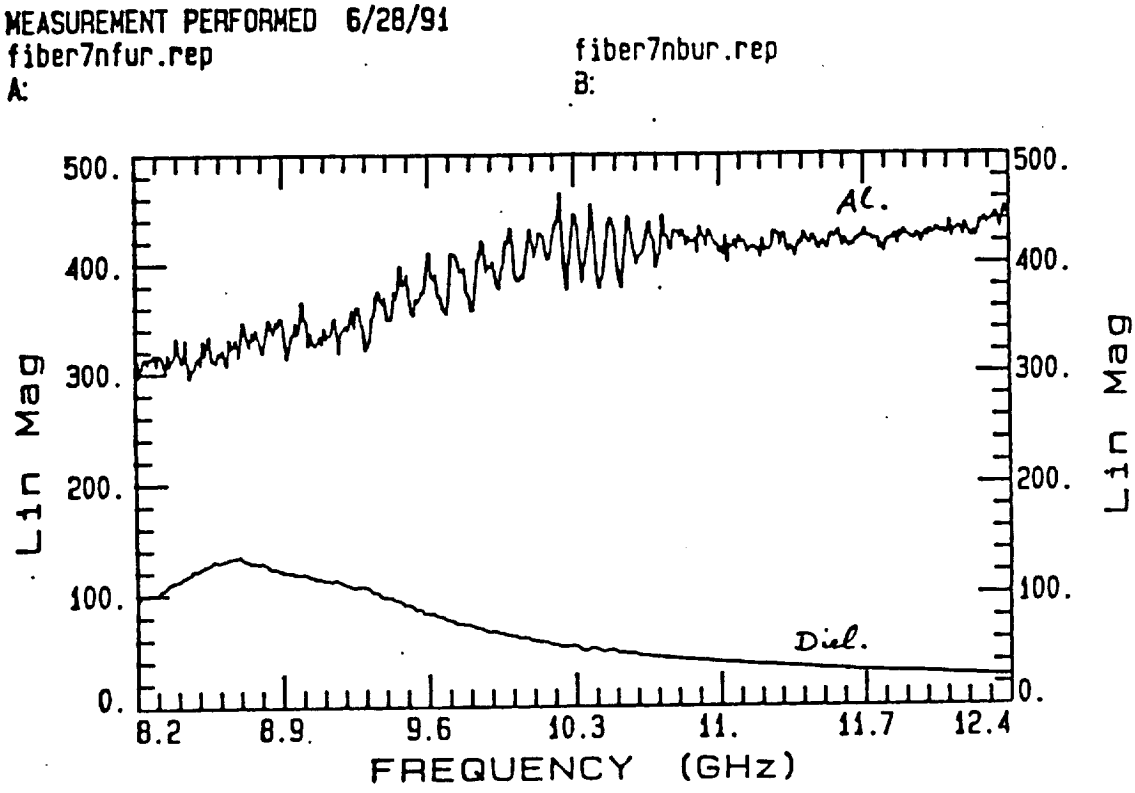

Figure 4: Conductivity of the SRI fiberglass sample with one aluminum screen at the surface.

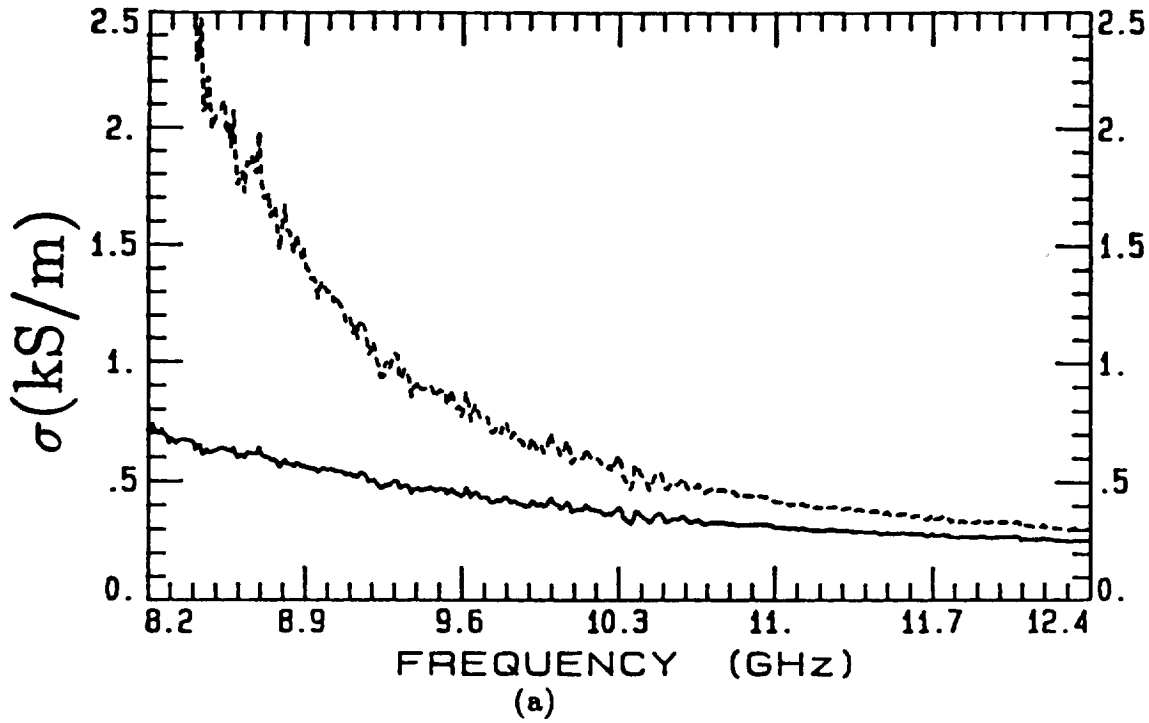

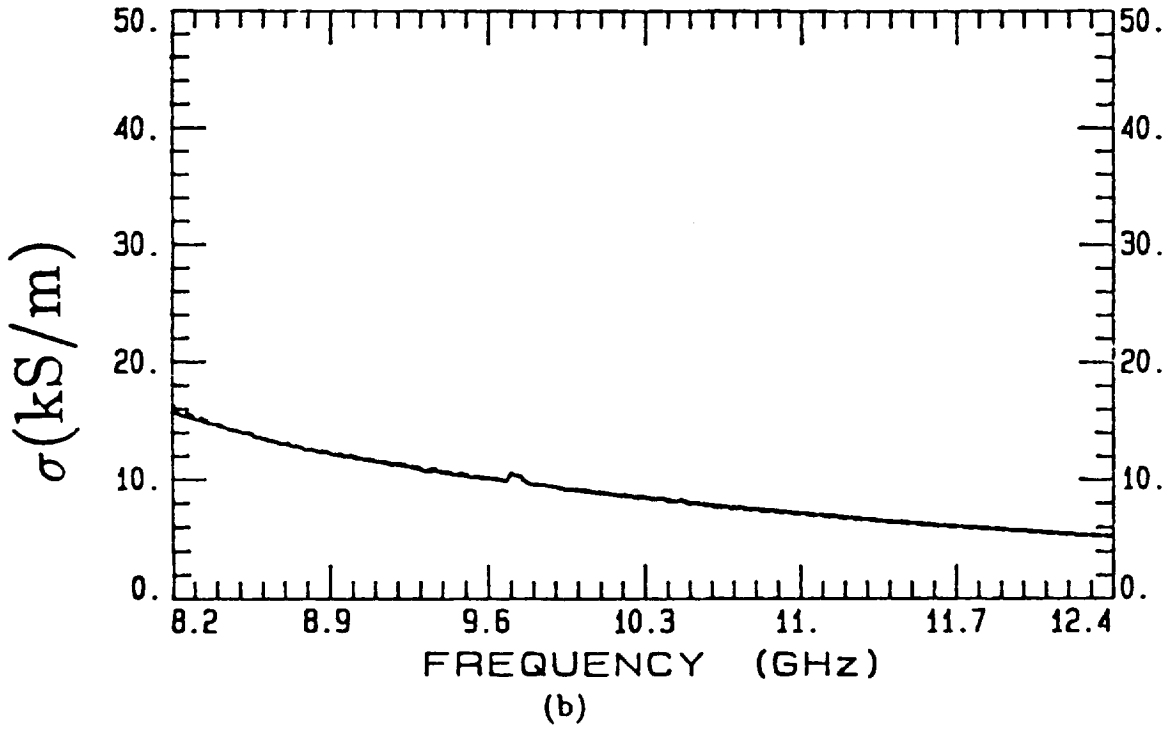

Figure 5: Conductivity of the Sikorsky fiberglass with two Aluminum screens, where Solid line: 45°; Dotted line: 0°. **a.** Screen side, **b.** Dielectric side.

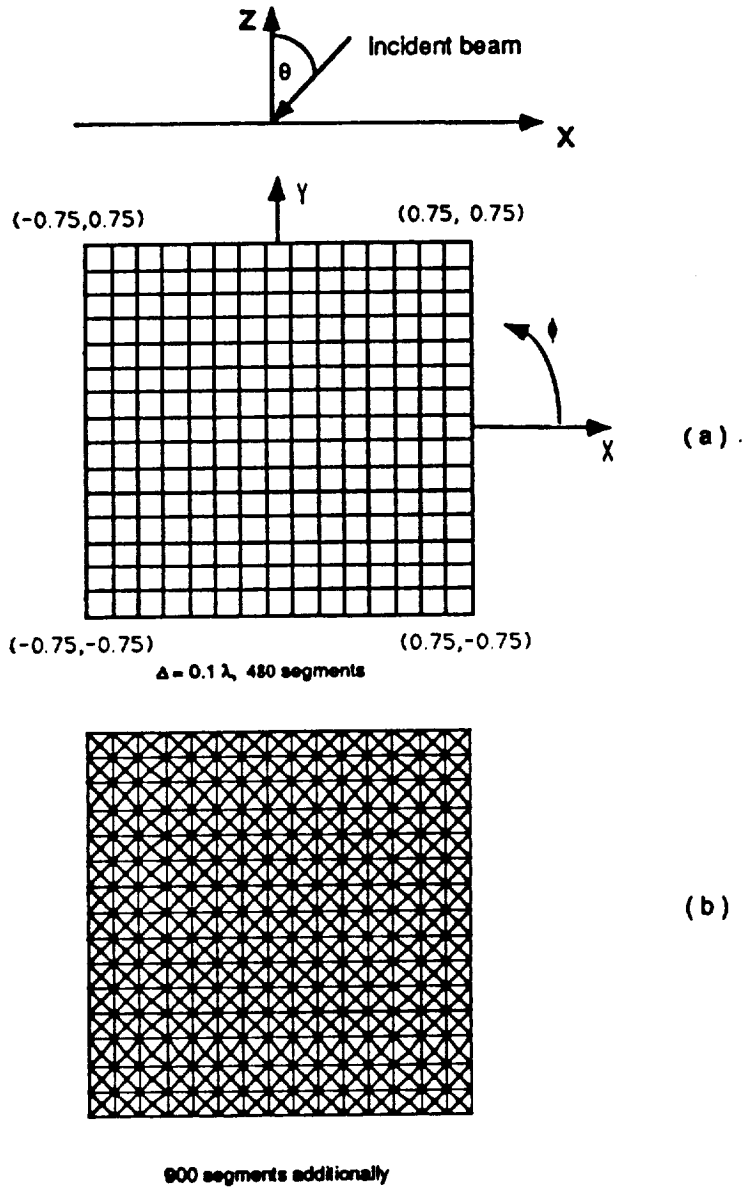

Figure 6: Wire grid representing a composite material sheet. **a.** Square mesh. **b.** Denser mesh.

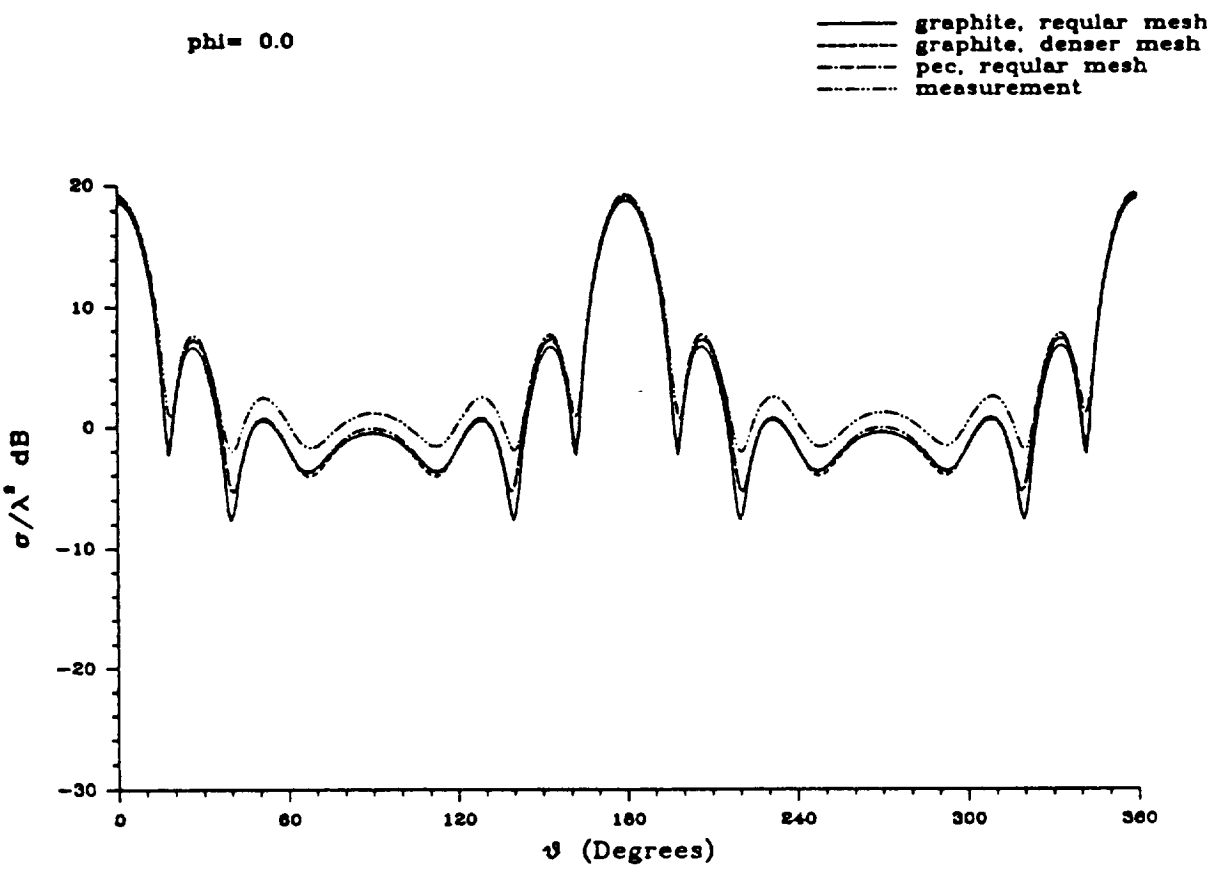

Figure 7: Principal elevation plane(0°) scattering pattern of a $1.5\lambda \times 1.5\lambda$ plate(soft polarization).

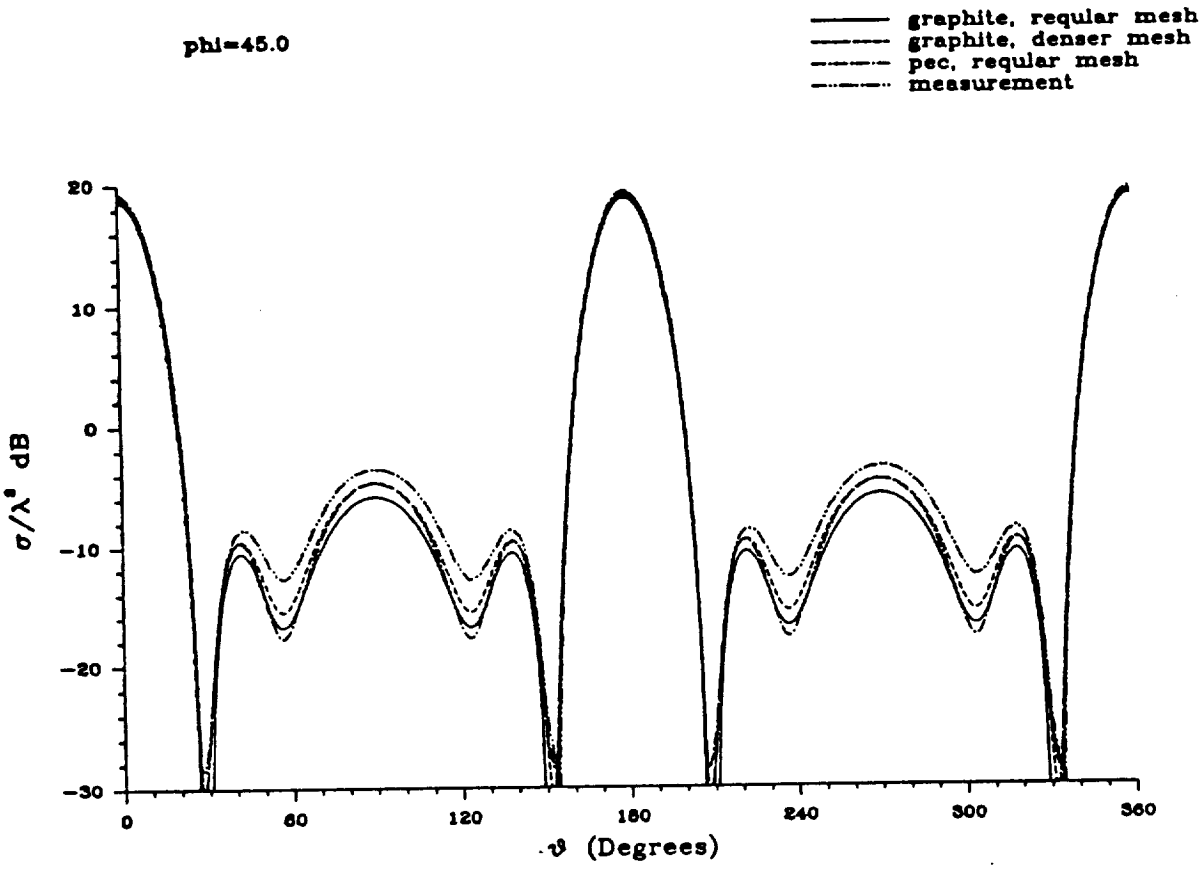

Figure 8: Oblique elevation plane(45°) scattering pattern of a $1.5\lambda \times 1.5\lambda$ plate(soft polarization).

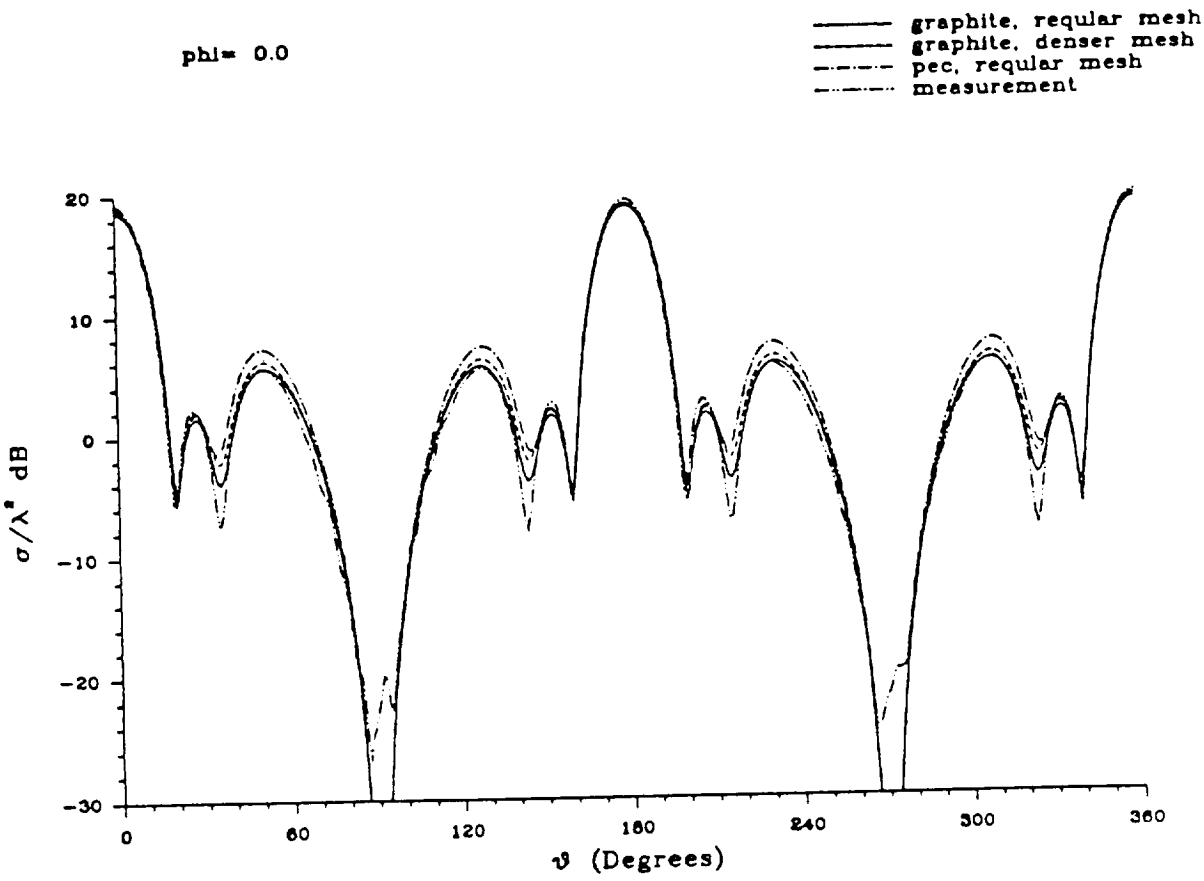

Figure 9: Principal elevation plane(0°) scattering pattern of a $1.5\lambda \times 1.5\lambda$ plate(hard polarization).

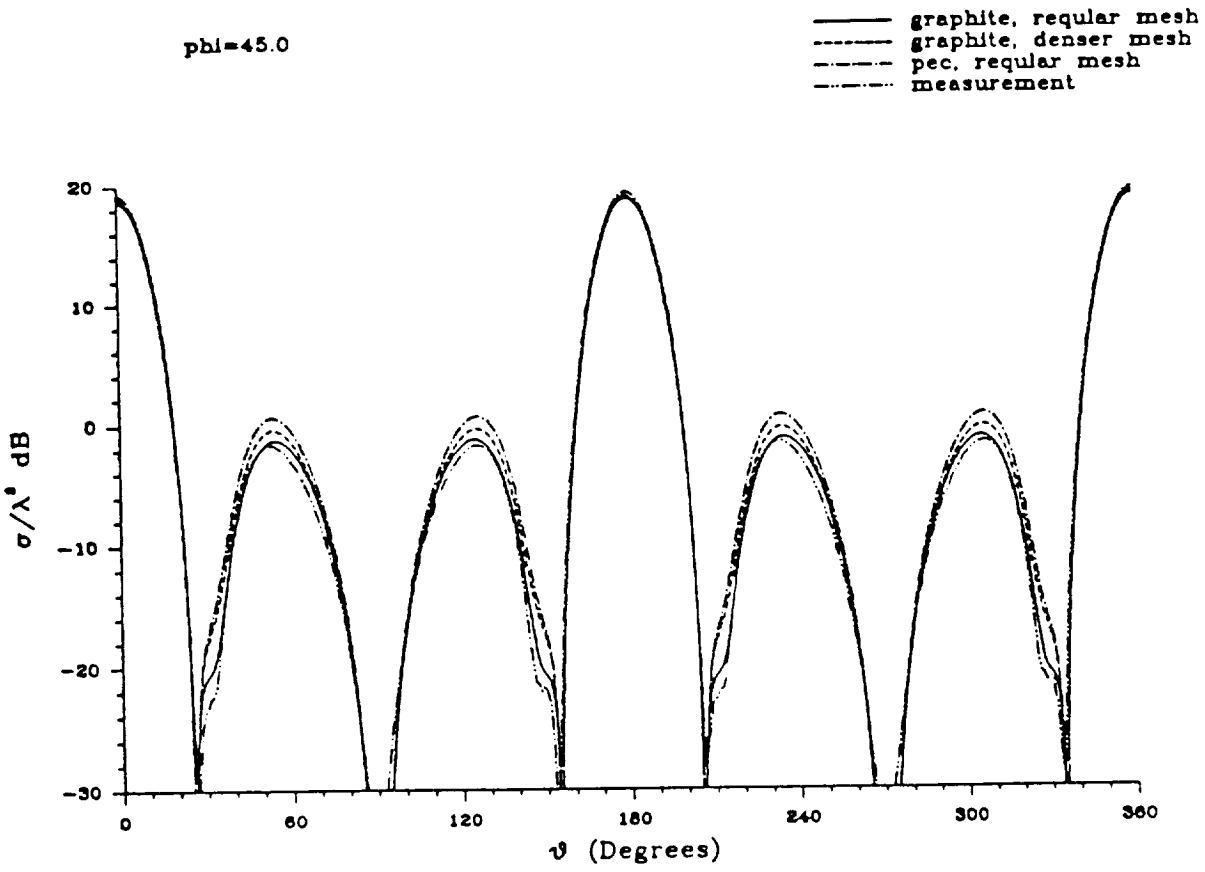

Figure 10: Oblique elevation plane(45°) scattering pattern of a $1.5\lambda \times 1.5\lambda$ plate(hard polarization).

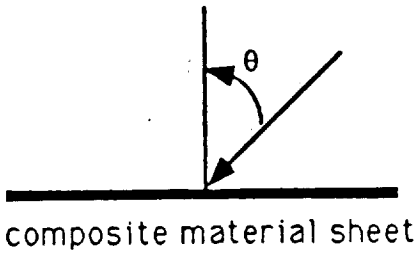

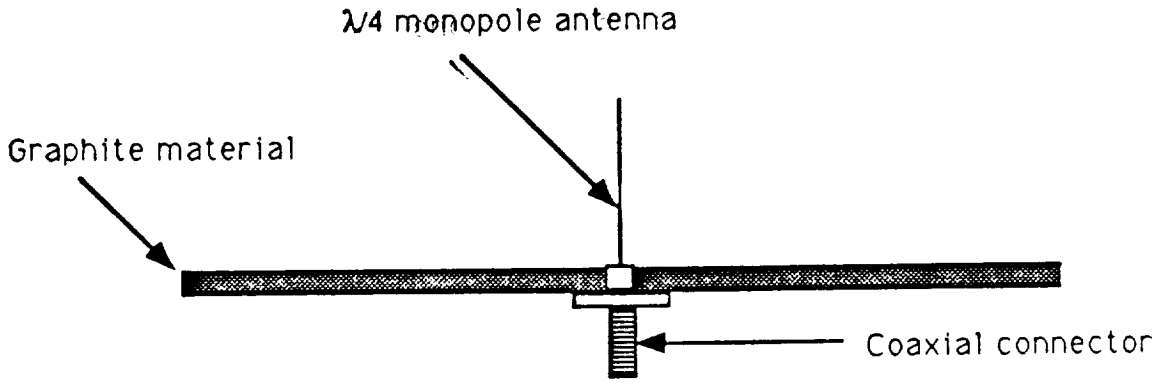

Figure 11: Geometry of a monopole antenna on a graphite material ground plane.

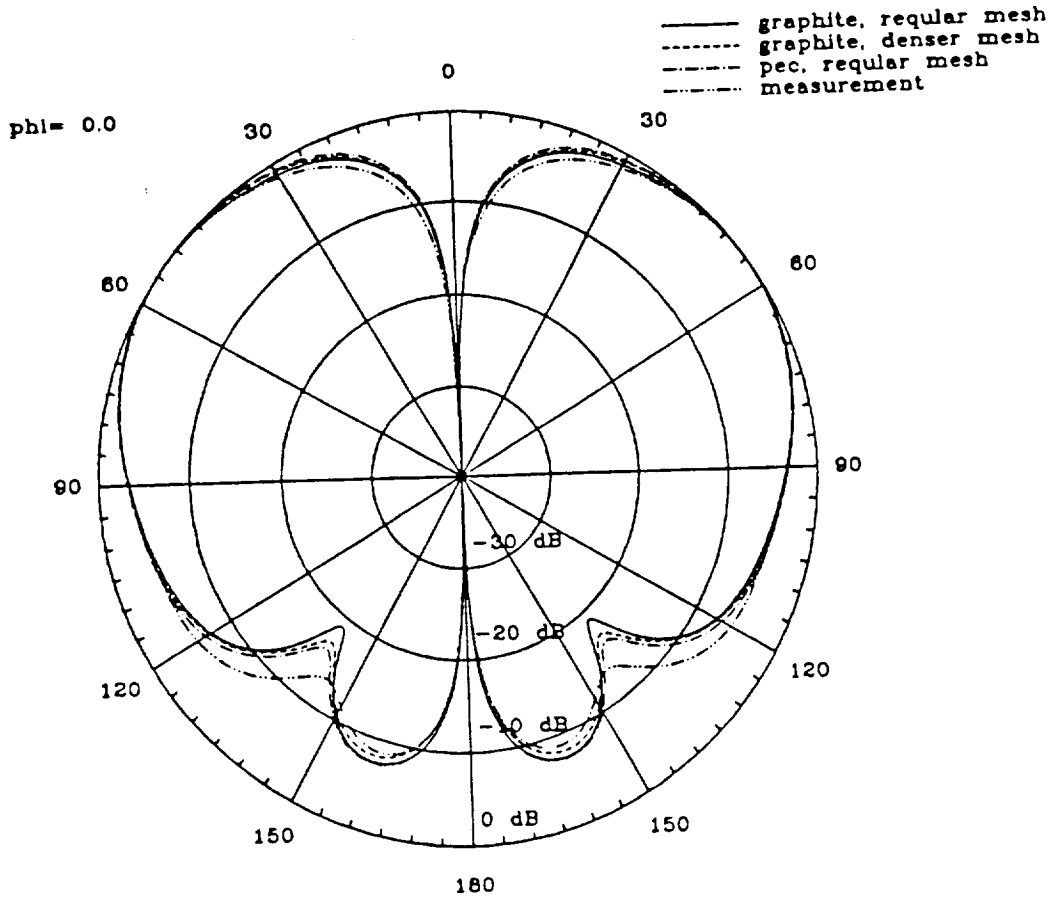

Figure 12: Principal elevation plane(0°) radiation pattern of a $\lambda/4$ monopole on a $1.5\lambda \times 1.5\lambda$ ground plane(co-polarization).

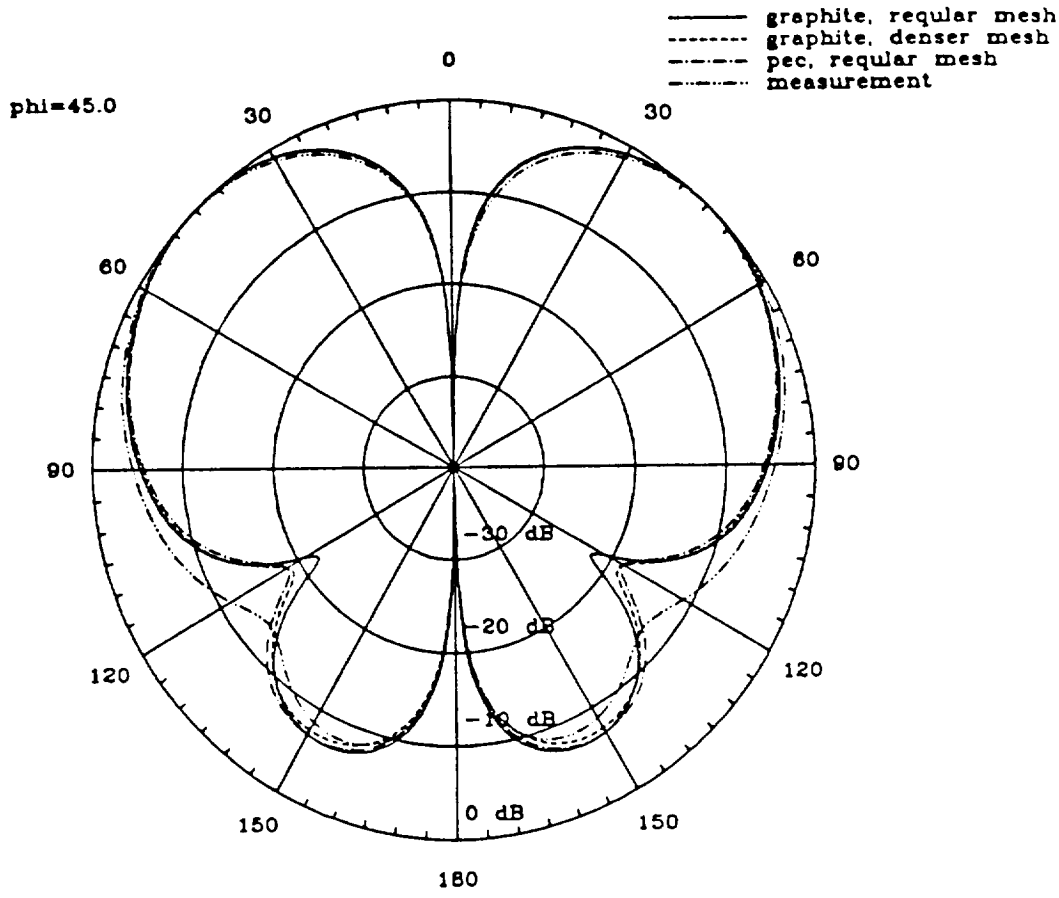

Figure 13: Oblique elevation plane(45°) radiation pattern of a $\lambda/4$ monopole on a $1.5\lambda \times 1.5\lambda$ ground plane(co-polarization).

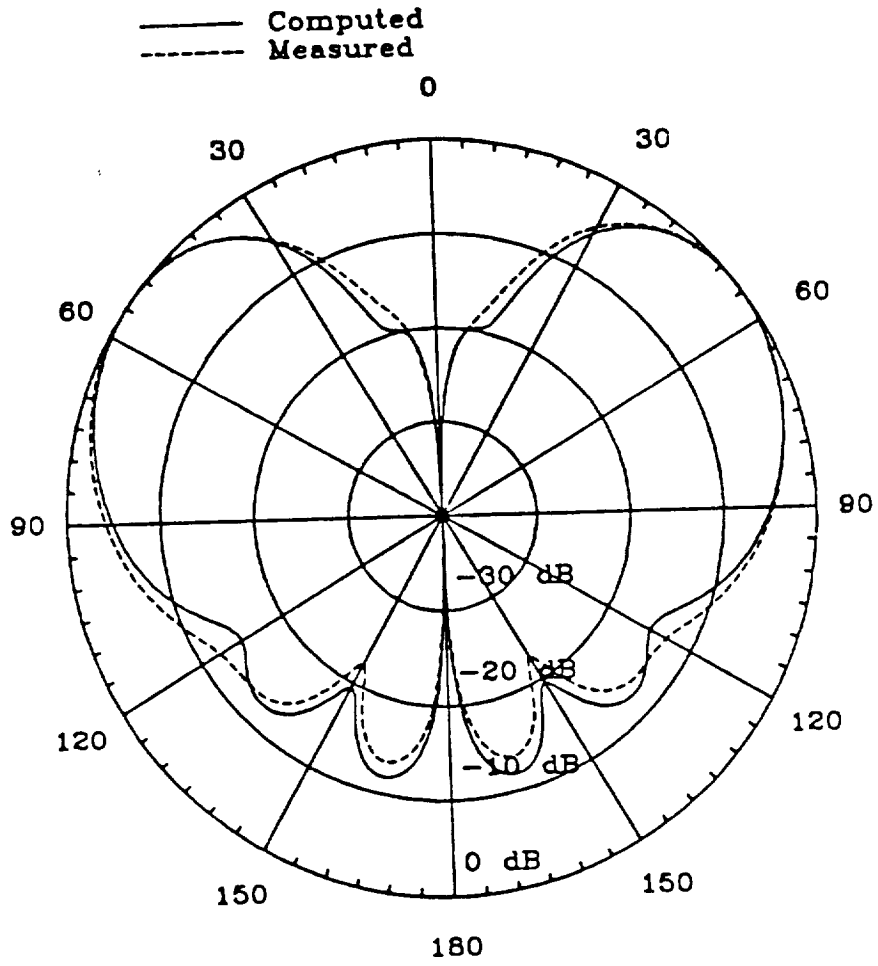

Figure 14: Radiation pattern of a quarter-wavelength monopole on a 2λ by 2λ plate. Impedance = (5 + j5).

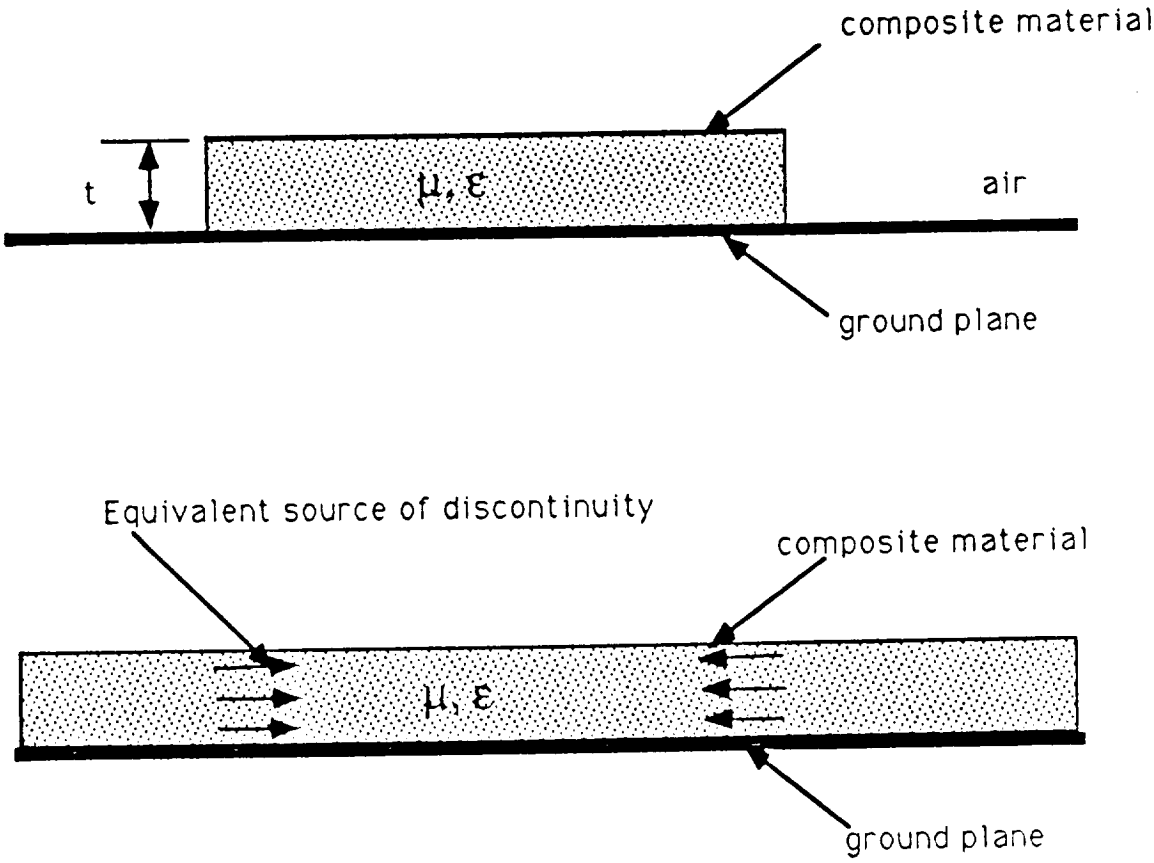

Figure 15: Analysis of discontinuities using the equivalent source.

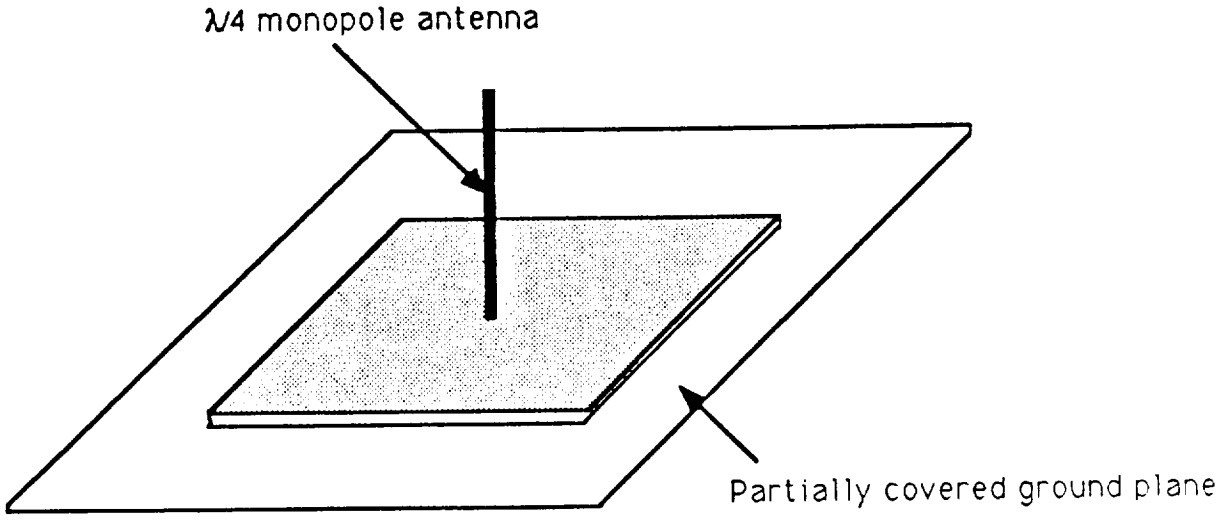

Figure 16: Geometry of a monopole antenna and partially-covered ground plane.

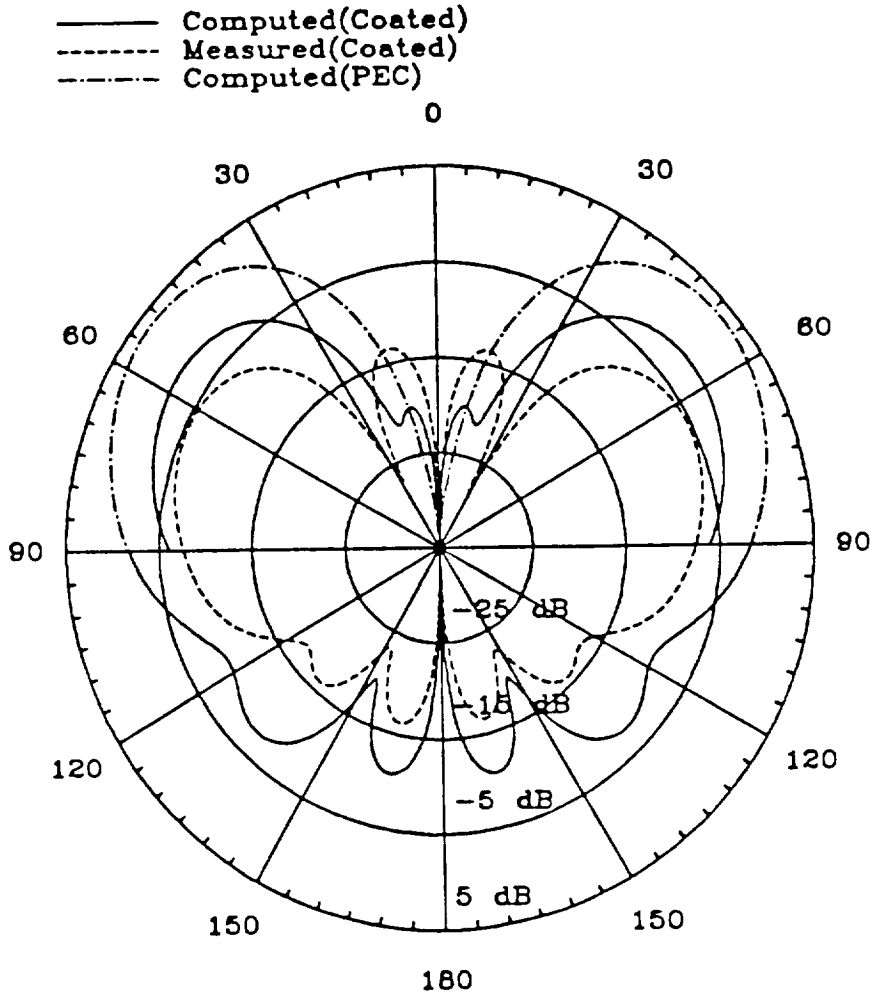

Figure 17: Radiation pattern of a quarter-wavelength monopole on a 2λ by 2λ coated plate.

III. Voltage Finite-Difference Time Domain Analysis of Corona Discharge Problem

A. Introduction

In the previous quarterly report, a simplified two-dimensional Voltage Finite-Difference Time-Domain code was developed to analyze *TE*-wave propagation in an infinitely long microstrip line structure, as shown in Figure 18. The program was limited since longitudinal propagation of the wave (Z-direction) had not been taken into consideration. Nevertheless, the general behavior of the fields and the surface current on and around the upper strip conductor were found to be reasonable. In the present report both longitudinal and transverse wave propagations are considered.

The report consists of two parts. In the first part, we are concerned with the extension of the longitudinal wave propagation in the Voltage FD-TD code for the microstrip line, and the dependency of its propagation on the operating frequency. The result obtained will be analyzed and verified by a different analytical method. In the second part, the Voltage FD-TD will be modified to determine radiation of a high voltage transmission line, shown in Figure 19, with and without air chemistry formulation [1] for the corona discharge, and the subsequent electromagnetic interference.

B. Voltage Finite Difference-Time Domain analysis of travelling wave along microstrip transmission line

In the absence of the dielectric substrate between the two conductors of a microstrip transmission line, the propagation constant of the wave travelling along the line is that of free space, and the characteristic resistance (assuming zero loss for the conductors) is independent of frequency. Inclusion of the dielectric substrate creates non-linear effects in the the propagation constant where it is no longer proportional to the frequency, and the characteristic impedance does not remain constant as a function of frequency. The non-linear effects are due to higher order *TE* (transverse electric) and *TM* (transverse magnetic) modes along the microstrip structure. To take into account the higher order modes and the longitudinal propagation constants, one needs to

include the $\vec{E}$ and $\vec{H}$ six components into the Voltage FD-TD program while they propagate along Z-direction.

To begin with, consider the most general three dimensional problem for $\vec{E}$ and $\vec{H}$ fields. They can be derived via auxiliary potentials V (scalar electric potential) and $\vec{A}$ (vector magnetic potential):

$$\vec{E} = -\vec{\nabla}V - \frac{\partial \vec{A}}{\partial t} \tag{5}$$

$$\vec{H} = \frac{1}{\mu}\vec{\nabla} \times \vec{A} \tag{6}$$

Both V and $\vec{A}$ are solutions to non-homogeneous second order partial differential equations

$$\nabla^2 \vec{A} - \mu\epsilon\frac{\partial^2 \vec{A}}{\partial t^2} = -\mu\vec{J}_t \tag{7}$$

$$\nabla^2 V - \mu\epsilon\frac{\partial^2 V}{\partial t^2} = -\frac{\rho_t}{\epsilon} \tag{8}$$

In addition, the pairs (V , $\vec{A}$), and ($\vec{J}, \vec{E}$) are related by

$$\vec{\nabla} \cdot \vec{A} + \mu\epsilon\frac{\partial V}{\partial t} = 0 \tag{9}$$

$$\vec{J} = \sigma\vec{E} \tag{10}$$

$\vec{J}_t$ and ρ_t can be external impressed sources that produce electromagnetic fields and/or internal response sources produced by the electromagnetic fields in the conductors (equation 10).

It is easily verified that any twice differentiable function of $(t - \frac{z}{u})$ or $(t + \frac{z}{u})$ can be the solution to *homogeneous* forms of equations (7) and (8) for a wave traveling in the positive or negative Z-directions, respectively. $u = \frac{1}{\sqrt{\mu\epsilon}}$ is the velocity of wave propagation in the medium with ϵ and μ as its permittivity and permeability, respectively. For the microstrip line the phase velocity lies between the speed of the light in free space ($\frac{1}{\sqrt{\mu_0\epsilon_0}}$) and the unbounded dielectric ($\frac{1}{\sqrt{\mu\epsilon_d}}$). Assuming the fields, the currents, and the potentials can be represented by the following general separable function

$$\vec{C}_0(x,y,z,t) = \vec{C}(x,y,t)f(t-\frac{z}{u}) \tag{11}$$

the three-dimensional problem can be reduced to a two-dimensional one, further minimizing the complexity of the analysis. For example,the FD-TD form of the electric field components become

$$E_x^{n+\frac{1}{2}}(i+\frac{1}{2},j) = -\frac{V^{n+\frac{1}{2}}(i+1,j)-V^{n+\frac{1}{2}}(i,j)}{\Delta x} - \frac{A_x^n(i+\frac{1}{2},j)-A_x^{n-1}(i+\frac{1}{2},j)}{\Delta t} \tag{12}$$

$$E_y^{n+12}(i,j+\frac{1}{2}) = -\frac{V^{n+\frac{1}{2}}(i,j+1)-V^{n+\frac{1}{2}}(i,j)}{\Delta y} - \frac{A_y^n(i,j+\frac{1}{2})-A_y^{n-1}(i,j+\frac{1}{2})}{\Delta t} \tag{13}$$

$$E_z^{n+\frac{1}{2}}(i,j) = \frac{1}{u}V^{n+\frac{1}{2}}(i,j) - \frac{A_z^n(i,j)-A_z^{n-1}(i,j)}{\Delta t} \tag{14}$$

Based on these equations a Voltage FD-TD code was developed to determine the propagation constant and characteristic resistance of the microstrip line structure shown in Figure 18. The flow chart used in this development is similar to the chart in the previous report. Figure 20 shows the characteristic resistance versus frequency for $w = 2mm$, $d = 2mm$, and $\epsilon_r = 2.5$. As it can be seen the characteristic resistance is a non-linear function of frequency which is due to the higher order TM modes propagating along the line. Figure 21 displays the normalized propagation constants versus normalized thickness for the TE and TM waves. β and k_0 are the propagation constants of the microstrip line and free space, respectively; and λ_0 is the wavelength in free space. TM_V and TE_V lines correspond to the values of $\frac{\beta}{k_0}$ versus $\frac{d}{\lambda_0}$ resulted from the Voltage FD-TD simulation. They are obtained from two different values of u computed by imposing the continuity of tangential electric field at the interface between the free space and the dielectric substrate. TM_T and TE_T lines present theoretical allowable $\frac{\beta}{k_0}$ versus $\frac{d}{\lambda_0}$ values for the higher order TE and/or TM modes in the dielectric substrate

without the upper strip conductor, which is often referred to as *slow wave structure*. These theoretical plots are obtained using the following iterative equations [2]:

$$tan\left(\left[\frac{\epsilon}{\epsilon_0}-\left(\frac{\beta}{k_0}\right)^2\right]^{\frac{1}{2}}k_0 d\right)=-\left(\frac{(\epsilon/\epsilon_0)-(\beta/k_0)^2}{(\beta/k_0)^2-1}\right)^{\frac{1}{2}} \tag{15}$$

for TE waves, and

$$tan\left(\left[\frac{\epsilon}{\epsilon_0}-\left(\frac{\beta}{k_0}\right)^2\right]^{\frac{1}{2}}k_0 d\right)=\frac{\epsilon}{\epsilon_0}\left(\frac{(\beta/k_0)^2-1}{(\epsilon/\epsilon_0)-(\beta/k_0)^2}\right)^{\frac{1}{2}} \tag{16}$$

for TM waves. As it can be seen, the computed normalized propagation constants by the Voltage FD-TD, and the iterative equations (15) and (16) are in good agreement.

C. Voltage FD-TD simulation of simplified corona discharge

In this section an attempt is made to implement a simplified version of corona discharge mechanism, using air chemistry formulation [1], into the Voltage FD-TD code, and to simulate the interference produced by the discharge. The model used for the simulation consists of an infinitely long two-wire transmission line immersed in an ionized medium, while a high potential gradient exists between the two wires. Furthermore, the wires are assumed to be square in their cross sectional view, as shown in Figure 19. There are two reasons for selecting this model. First, the elongated sharp corners of the wires can approximate some of the sharp edges on the body of an aircraft, where high electric fields are more prevalent. Second, the two-dimensional set up of the model simplifies the program and its running time when the additional air chemistry formulation is implemented.

To observe the effect of the simplified corona discharge on the radiated wave from the transmission line two different conditions were simulated using the Voltage FD-TD program. In the first condition Voltage FD-TD was used to determine the radiated electric and magnetic fields without the air chemistry formulation. This is similar to first half of the present report

without the dielectric substrate. In the second situation, the air chemistry formulation was used to modify the Voltage FD-TD code to find the radiated electric and magnetic fields.

The three-species air chemistry formulation for n_e electron density $[\frac{1}{cm^3}]$, n_- negative ion density $[\frac{1}{cm^3}]$, and n_+ positive ion density $[\frac{1}{cm^3}]$ is given by the following differential equations:

$$\frac{dn_e(t)}{dt} + \left[\beta n_+(t) + \alpha_e(|\vec{E}(t)|) - G(|\vec{E}(t)|)\right] n_e(t) = Q(t) \tag{17}$$

$$\frac{dn_-(t)}{dt} + \gamma n_+(t) n_-(t) = \alpha_e(|\vec{E}(t)|) n_e(t) \tag{18}$$

$$\frac{dn_+(t)}{dt} + \left[\beta n_e(t) + \gamma n_-(t)\right] n_+(t) = Q(t) + G(|\vec{E}(t)|) n_e(t) \tag{19}$$

$$n_+(t) = n_e(t) + n_-(t) \tag{20}$$

$$\sigma = q(\mu_e n_e + \mu_- n_- + \mu_+ n_+) \tag{21}$$

where β is the lumped electron-ion recombination $[\frac{cm^3}{sec}]$, α_e is the lumped electron attachment rate $[\frac{1}{sec}]$ as a function of electric field, γ is the lumped ion-ion neutralization coefficient $[\frac{cm^3}{sec}]$, G is the avalanche rate $[\frac{1}{sec}]$ as a function of electric field, and Q is the ionization rate $[\frac{ion-pairs}{cm^3}]$. σ is the air conductivity $[\frac{mhos}{cm}]$, μ_e, μ_-, and μ_+ are the electron, the negative ions, and positive ions mobilities, respectively. Figure 22 displays the flow chart that was used to develop the modified Voltage FD-TD program. The steps in the flow chart are similar to the previous report flow chart with the additional variable conductivity at every point (except the conductors) to be computed and used at every cycle of the program. Figure 23 shows the radiated electric field at some point between the conductors of the transmission line. Solid line presents the variation of the electric field as a function of time without the air chemistry formulation. The frequency of the excitation was set to 2.5 GHz. The line indicates smooth variation of the electric field as a sinusoidal potential difference are excited on the transmission line. Dashed line represents the electric field as a function of time with the air chemistry formulation. High oscillatory variation of the dashed line shows interference due to variable conductivity, or change in the electron and ion densities (equation

21), in the area surrounding the wires which indicates the corona discharge. This is an important result since spectrum analysis of the electric field can reveal some of the possible electromagnetic interference (EMI) frequencies produced by the air chemistry formulation, or the corona discharge.

D. Future work

For the future, our effort will be directed toward more accurate and complex modeling of the air chemistry formulation for the sharp wedge near an infinite ground plane where there is high electric potential between the wedge and ground plane. The high electric field intensity near the sharp wedge can be considered to be an excellent model to the high electric field near the sharp wedges of the wings of an aircraft or the rotary blades of a helicopter. Hence, EMI predicted by the model will give some indication on the frequency spectrum generated by the sharp edges of the aircraft, and how this spectrum will interfere with on-board communication systems.

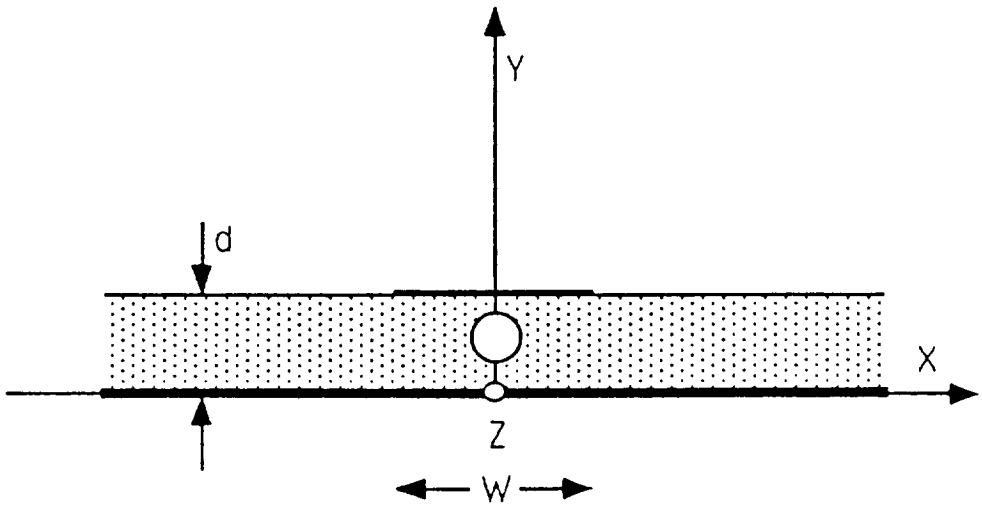

Figure 18: Microstrip transmission line excited by sinusoidal voltage source.

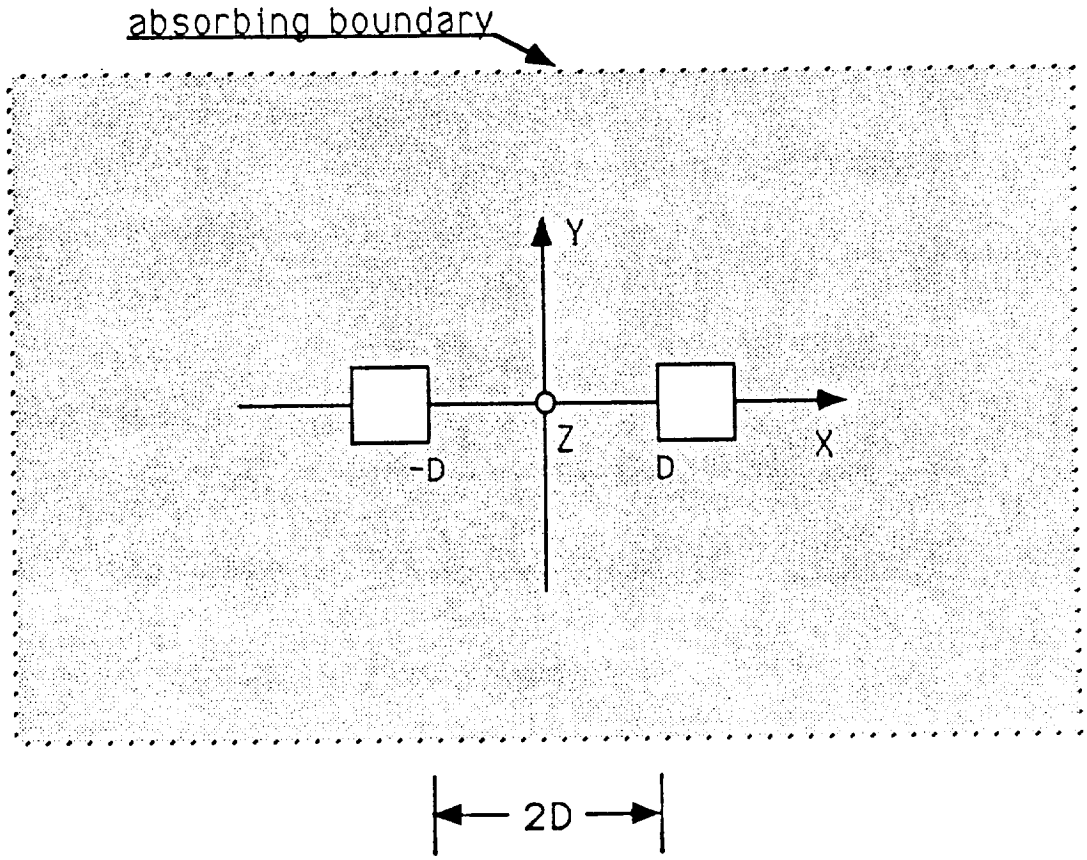

Figure 19: Two-wire transmission line used in the corona discharge analysis.

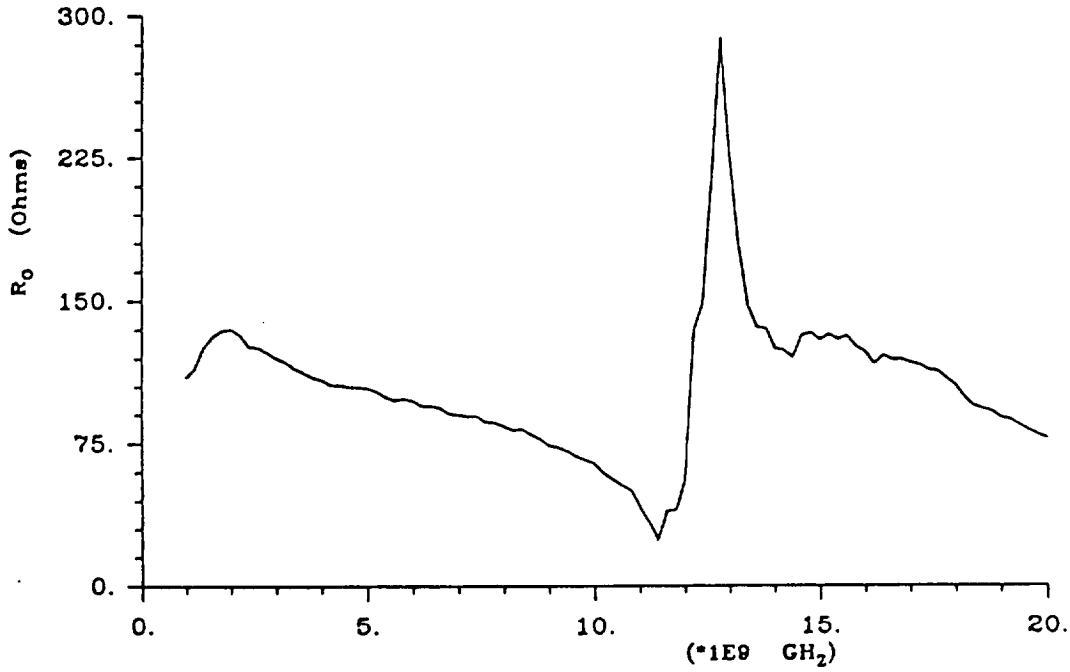

Figure 20: Characteristic resistance of the microstrip transmission line as a function of frequency for w =3.91 mm, d =1.27 mm, and $\epsilon_r = 2.2$.

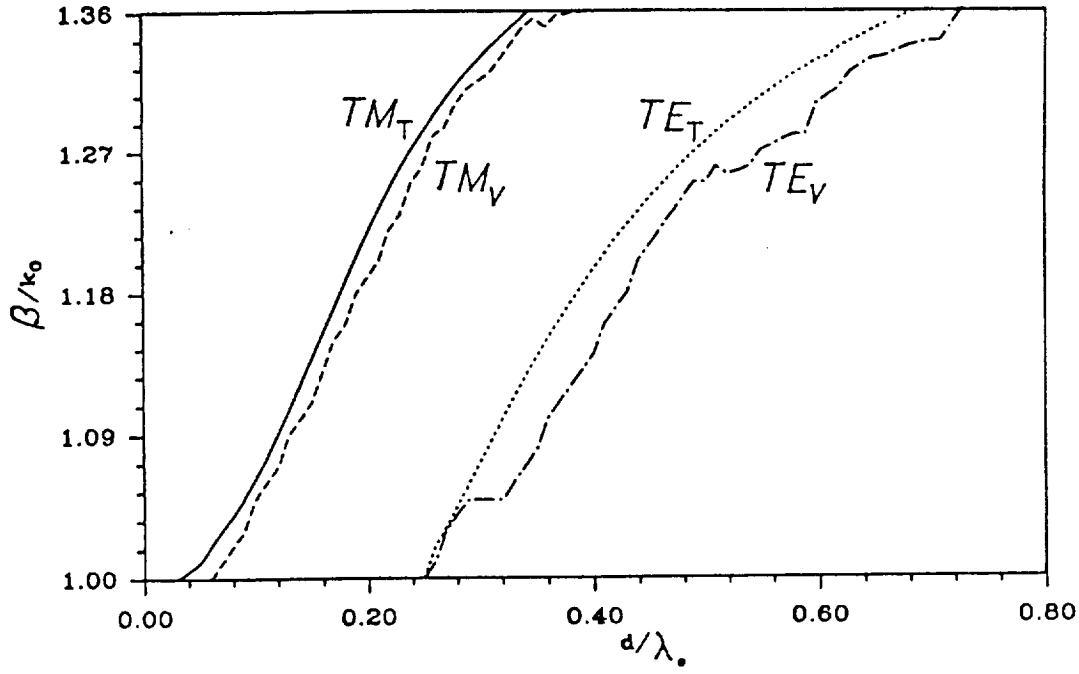

Figure 21: Normalized TE wave and TM wave propagation constants of the Microstrip Transmission Line and Dielectric-Clad ground plane as functions of normalized dielectric thickness.

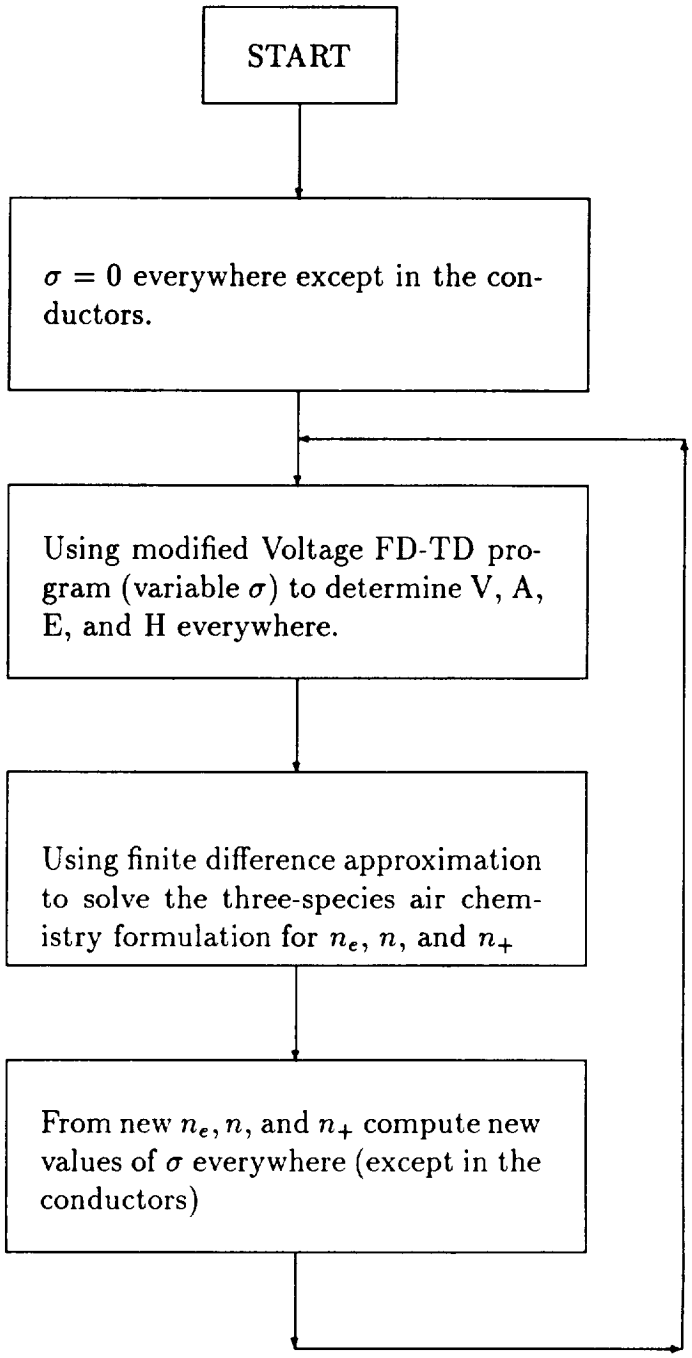

Figure 22: Flow chart for the modified Voltage FD-TD analysis of the corona discharge.

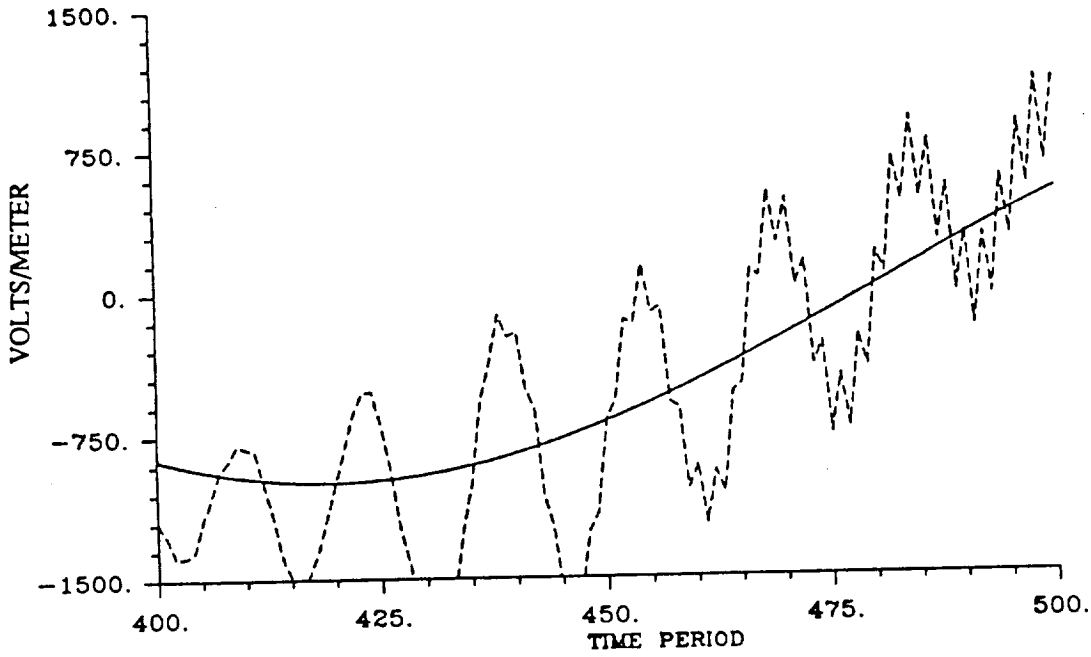

Figure 23: Computed X-directed electric field at x=D/4, where the dashed line represents the formulation with the air chemistry and the solid line is that without the air chemistry.

IV. ANTENNA TECHNOLOGY

A. Introduction

Microstrip and cavity-backed slot antennas are widely used at UHF and above in aerospace applications such as helicopters because they are conformal to the vehicle surface as well as light weight, low cost and easy to manufacture. During the past year, significant progress has been made in three areas of conformal antenna technology: **polarization-diverse microstrip antennas, ferrite-loaded cavity-backed slot antennas and varactor-tuned microstrip patch antennas.** In this section, progress to date in each of these areas is discussed, and plans for future work are outlined.

B. Polarization-Diverse Conformal Microstrip Patch Antennas

During the first two years of the AHE program, we developed numerical codes for the analysis of two-probe-fed rectangular and circular microstrip patch antennas fed by resistive and reactive power divider networks. These solutions utilize a rigorous full-wave Green's function/Galerkin approach, and thus model all of the effects of the dielectric substrate (including surface waves) as well as feed-to-feed coupling. Such a rigorous approach must be used if the models are to be accurate for patches printed on thick and/or high dielectric constant substrates. Another important consideration is the fact that the frequency performance of these patch radiators depends on the characteristics of the specific network chosen to feed the element. Hence, a rigorous analysis that accurately treats both the patch radiator and its feed network is imperative. These codes can be used to evaluate the overall performance of polarization diverse conformal antennas in terms of return loss, axial ratio, cross-polarization level or polarization mismatch.

Figure 24 illustrates the geometry of two-probe-fed circular microstrip patch antenna. The antenna was fabricated at ASU using our newly developed printed circuit fabrication facility. The antenna parameters are $\epsilon_r = 2.33, tand = 0.0012, d = 0.21844$ cm, $R = 2.0$ cm, $x_{p1} = 0.7$ cm, $y_{p1} = 0, x_{p2} = 0, y_{p2} = 0.7$ cm, $r_0 = 0.045$ cm. The start frequency is 2.0 GHz, the stop frequency is 3.0 GHz, and the frequency step is 25 MHz. The measured scattering parameters (S_{11} and S_{21}) for the antenna are compared

in Figure 25 to results calculated using the numerical model. The calculated data was obtained using 326 seconds of CPU time on ASU's Cray X-MP/18se supercomputer. Measurements were made in ASU's ElectroMagnetic Anechoic Chamber (EMAC) facility. As can be seen, the agreement between theory and experiment is quite good.

C. Ferrite-Filled Cavity-Backed Slot Antennas

We reported our efforts on the cavity-backed slot antennas in the previous semiannual progress report. Since then, further progresses have been made and they are represented in this progress report.

Narrow bandwidth is a major disadvantages of conventional microstrip and cavity-backed slot antennas. This disadvantage precludes their use in a number of applications that could benefit from antennas possessing their many desirable characteristics. In this and the next section, we discuss some of the efforts underway to develop tunable conformal antennas. The basic concept is to start with an inherently narrow-bandwidth antenna and somehow vary one of its parameters allowing the antenna to be tuned over a fairly wide bandwidth. In many applications, it is actually more desirable to use such a tunable, inherently narrow-bandwidth antenna than an inherently wide-bandwidth antenna because of the ability of the narrow-bandwidth antenna to reject out-of-band interference.

The use of magnetized ferrite to control radiation and scattering characteristics of antennas is a promising yet relatively undeveloped technology. One can conceive of a cavity-backed slot antenna that could be used to cover several different frequency ranges if materials of different constitutive parameters were substituted into the cavity backing. In practice, this concept can be realized by partially (or completely) filling the cavity with ferrite and then varying the permeability tensor of the ferrite by application of an external magnetic field.

An example of the type of structure we are considering is shown in Figure 26. A radiating slot is etched in the ground plane of a printed microstrip feed network and backed by a cavity which contains both ferrite and dielectric layers. We have fabricated a prototype antenna with the following parameters:

- CAVITY: 0.60 in $\times$ 0.40 in $\times$ 0.25 in.

- FERRITE:
  $4\pi M_s = 3400\ Gauss$
  $\epsilon_r = 15.5$
  $linewidth = \Delta H = 600\ Oe$
  $thickness = 0.025\ in.$

- DIELECTRIC:
  $\epsilon_r = 10.8$
  $thickness = 0.050\ in$

Figure 27 shows the return loss and insertion loss seen by the microstrip line. There are three distinct response regions: the first from 5 GHz to 7 GHz, the second from 8.5 GHz to 9.5 GHz, and the third from 10 GHz to 10.5 GHz. The first region is due to complex air-guided magnetostatic surface waves which occur at frequencies above the resonant frequency

$$f_a = \gamma(H_0 + \frac{4\pi M_s}{2}) \tag{22}$$

which for this material is 4.76 GHz. The second region is due to complex ground-guided magnetostatic surface waves which occur at frequencies below the resonant frequency

$$f_g = \gamma(H_0 + 4\pi M_s) \tag{23}$$

which for this material is 9.52 GHz. The resonance of the cavity itself which occurs at 10.25 GHz is the dominant mechanism in the third region. For this ferrite material, the first two regions are not very useful for antenna purposes as there is very little radiation loss and measured patterns are quite poor. This can be attributed to the large line-width (600 Oe), which results in large loss near the resonant frequencies. Low loss materials have linewidths of 50 Oe or less, and can be as low as 1 Oe. On the other hand, the third region seems to be somewhat more useful for these purposes. Figure 28 shows the H-plane co-polarized radiation pattern of the antenna at 10 GHz. While the H-plane pattern is reasonably symmetric, measurements have shown that the E-plane pattern is substantially worse. Additional work needs to be done in this area.

It is expected that the development of analysis software for the structure will greatly enhance our ability to successful implement this novel antenna

concept. As a first step in the analysis of these types of antennas, full-wave numerical models for two-dimensional free-space-filled cavity-backed slot antennas have been developed. These models allow evaluation of the scattering width as well as the input admittance per unit length and radiation pattern of the antenna.

Figure 29 shows the geometry of a two-dimensional cavity-backed slot in an infinite, perfectly conducting, zero thickness ground plane. Full-wave Galerkin solutions for determining the scattering width and input admittance per unit length of this radiating structure have been developed. These solutions utilize the Green's function for a magnetic line current element radiating in the presence of an infinite, perfectly conducting ground plane. To facilitate the analysis, this Green's function is derived in the spectral domain. In addition, the Green's function for a magnetic line current element radiating into a two-dimensional cavity comprising perfectly conducting walls is also required.

To evaluate the scattering width, a plane wave is assumed to be incident upon the structure. The equivalence principal is used to close off the aperture and replace it with a magnetic surface current just above the ground plane and its negative just below the ground plane. This ensures continuity of the tangential electric field across the slot. The unknown magnetic surface current is obtained by formulating an integral equation statement of the boundary condition that the tangential magnetic field must be continuous across the slot. The integral equation is discretized by expanding the unknown magnetic surface current in a set of known basis functions with unknown coefficients and following Galerkin's procedure.

Two different sets of basis functions are considered. The first comprises a set of sinusoidal functions which do not explicitly exhibit the proper behavior near the knife edge. The second set of basis functions comprises Chebychev polynomials modified by an appropriate edge factor. Conveniently, the Fourier transforms of functions in both basis sets can be found in closed-form. Numerical studies have found that while both basis sets yield identical results, the basis set with proper edge behavior converges much more rapidly, and is thus the preferred basis set. However, the spectral domain integrations for the admittance matrix elements that arise from this basis set require convergence acceleration for accurate calculation to avoid unreasonably long calculation times.

Figure 30 shows the calculated scattering width of the slot in decibels

relative to one meter for both hard (TM_z) and soft (TE_z) polarizations. The antenna parameters are $W = 5.0$ cm, $\epsilon = 2.0, m_r = 1.0, a = 35.4$ cm, $c = 17.7$ cm, $\theta^i = 30$ degrees. Notice the peaks in the scattering response which correspond to the cavity resonances.

Figure 31 shows the calculated input admittance per wavelength of the slot. The parameters are the same as in Figure 30. For this calculation, the plane wave excitation is replaced by a current sheet in the aperture. Each of the curves in Figure 30 and the two curves in Figure 31 were calculated using about 220 seconds of CPU time on the Cray X-MP/18se.

We are currently extending our existing computer codes to allow treatment of a three-dimensional slot antenna backed by a cavity that is filled with arbitrary dielectric and ferrite layers.

D. Varactor-Tuned Microstrip Patch Antennas

The principle of the varactor-tuned patch antenna can be qualitatively explained as follows. Consider the equivalent circuit of a conventional circular patch based on the cavity model as shown in Figure 32. The R-L-C tank circuit represents the dominant mode of the patch with R representing all loss mechanisms (including radiation), and the series inductance represents higher order (non-radiating) modes of the patch as well as the effect of the probe feed. By mounting a varactor diode between the patch conductor and the ground plane, we effectively couple a voltage-controlled capacitance in parallel with the R-L-C tank circuit. By varying the voltage across the varactor, we change the capacitance of the tank circuit and thus the resonant frequency of the antenna.

The geometry of the varactor-tuned circular patch antenna that was fabricated is shown in Figure 33. A high Q silicon hyperabrupt tuning varactor (part number MA4ST556_31) was denoted by M/A-COM and used in the prototype. The probe feed position is chosen such that the patch has an input impedance close to 50 Ohms at resonance, and the position of the diode is near to where the maximum electric field occurs under the patch in order to maximize the amount of tuning. The DC bias supply is connected through the HP-8510 network analyzer. The input return loss versus frequency for several bias voltages is shown in Figure 34. As can be seen, in changing the bias voltage from 0 volts to 15 volts, we are able to tune the antenna from 1.575 GHz to 2.64 GHz, which corresponds to a 50% bandwidth.

A comparison of measured and calculated input return loss versus frequency for bias voltages of 4 and 20 volts is shown in Figure 35. The calculated data is generated using the computer program for two-probe-fed circular microstrip patch antennas mentioned earlier. The varactor diode is modeled as a lumped load at the base of a perfectly conducting pin whose radius is equal to the actual diode radius. The load impedance is evaluated from the equivalent circuit for the varactor diode shown in Figure 36. As can be seen, the agreement between theory and experiment is good. Tolerances in the dielectric constant of the substrate and patch dimensions combined with an inability to exactly specify the diode packaging parasitics are the likely causes of the slight deviations between theory and experiment.

E. Future Work

During 1992, work will continue on the topics discussed above. Using our rigorous models, it has been found that two-probe-fed circular and rectangular microstrip patch array elements which are designed to radiate and receive circular polarization exhibit axial ratios at boresight which are on the order of 1 to 2 dB. In many systems, these performance levels are unacceptable. During 1991, we began to investigate some techniques for improving the axial ratio. One approach is to use balanced pairs of probes to create a perfectly symmetrical radiator. This approach has the disadvantage of requiring a more complicated feed network, which may no longer be achievable using a purely planar structure. It is also possible to compensate for the element asymmetry by adjusting the amplitude and phase of the feed excitation by suitably designing the feed network. Another very interesting approach to be investigated during 1992 is the use of an gyromagnetic (ferrite) superstrate to achieve high-quality circular polarization from an element with an intrinsically poor axial ratio or even from a linearly polarized element.

Investigation of some stacked microstrip patch antenna configurations will also begin during the next quarter. By stacking patch antennas, one can improve the impedance bandwidth of the antenna and/or provide for an antenna which can operate at two widely separated frequencies.

During the past year, we began to investigate slot antennas backed by cavities that are partially filled with ferrite. Experiments to measure the radiation pattern and efficiency of a prototype cavity-backed slot antenna have been performed at microwave frequencies. The ferrite material that

was used in our experimental work has a line width of 600 Oe, and is thus not suitable for magnetostatic applications. There is considerable interest in using this type of antenna at VHF and UHF frequencies. We have contacted Trans Tech Co., and they have agreed to donate high quality ferrite materials suitable for operation in magnetostatic modes. In particular, we will be receiving TTVG-800 with a line width of 10 Oe, which will enable operation at UHF (1.1 GHz). Another material we will be receiving is G-1009 with a line of 50 Oe, which will enable operation at VHF (250 MHz).

Computer codes are currently under development to predict the performance of these antennas. These codes will utilize rigorous, fully electromagnetic approaches and should provide us with a good deal of insight on how to design these antennas for optimum performance. Both experimental and theoretical efforts will continue through 1992.

Work will also continue on characterizing varactor-tuned microstrip patch antennas. We are particularly interested in investigating the possibility of developing such antennas for the UHF range as well as enhancing our computer model with the ability to predict the radiation patterns of such antennas.

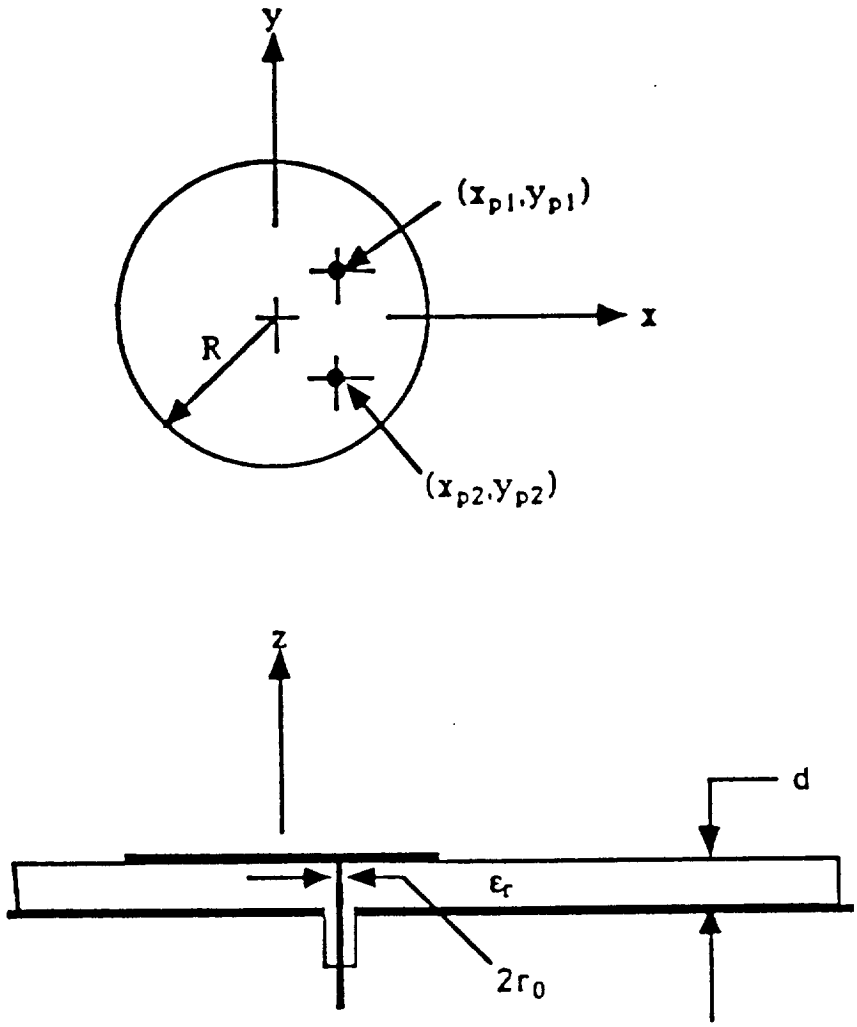

Figure 24: Geometry of a two-probe-fed circular microstrip patch antenna.

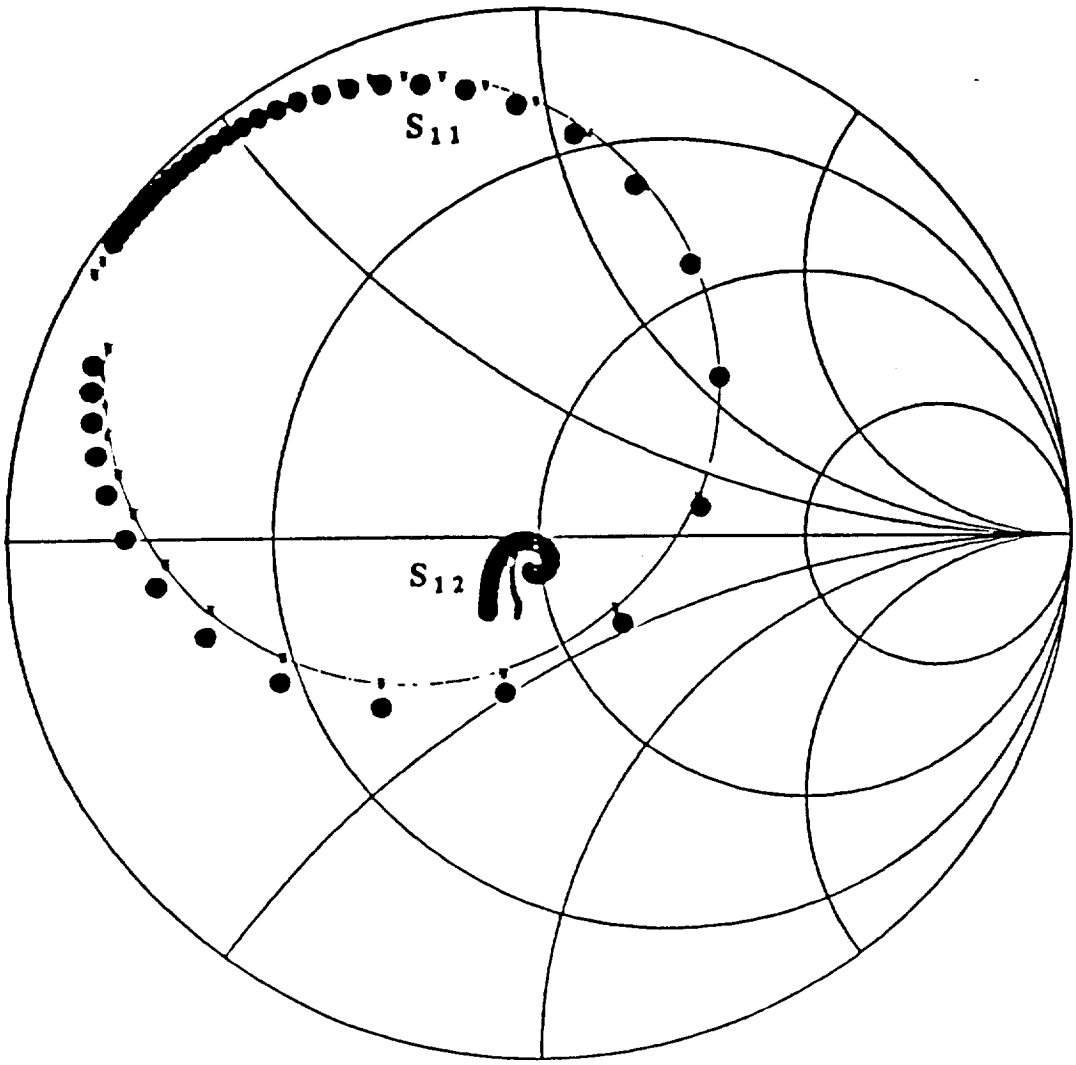

Figure 25: Measured and calculated S_{11} and S_{12} for a two-probe-fed circular patch antenna with the probe feeds positioned to provide unbalanced circular polarization.

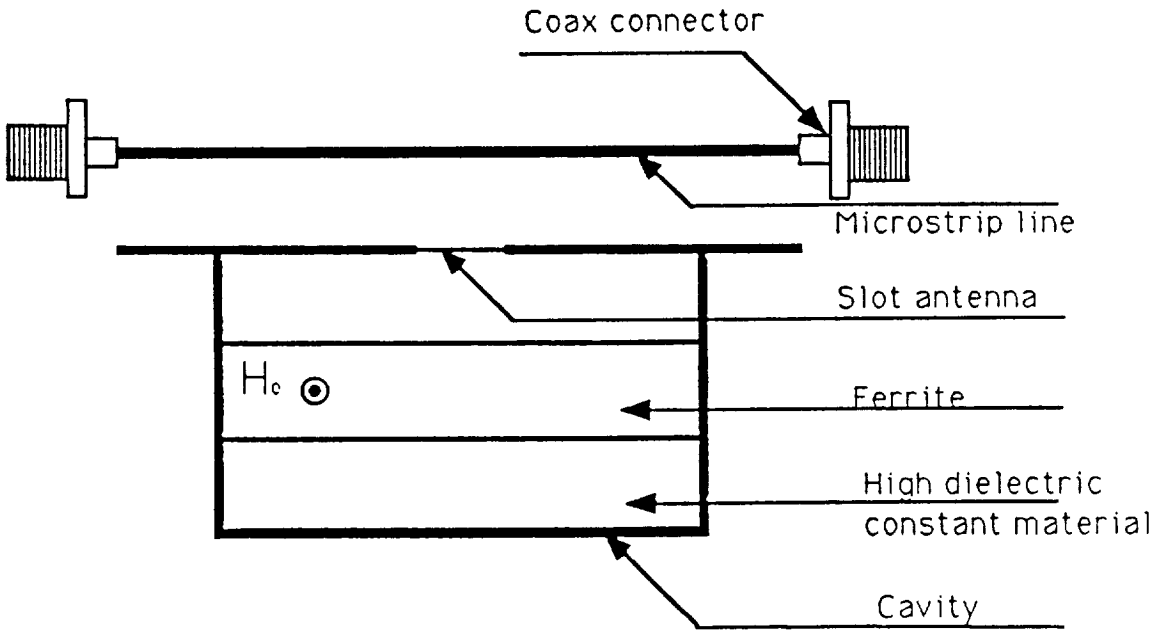

Figure 26: Cross-section of a slot radiator that is backed by a cavity containing a ferrite layer.

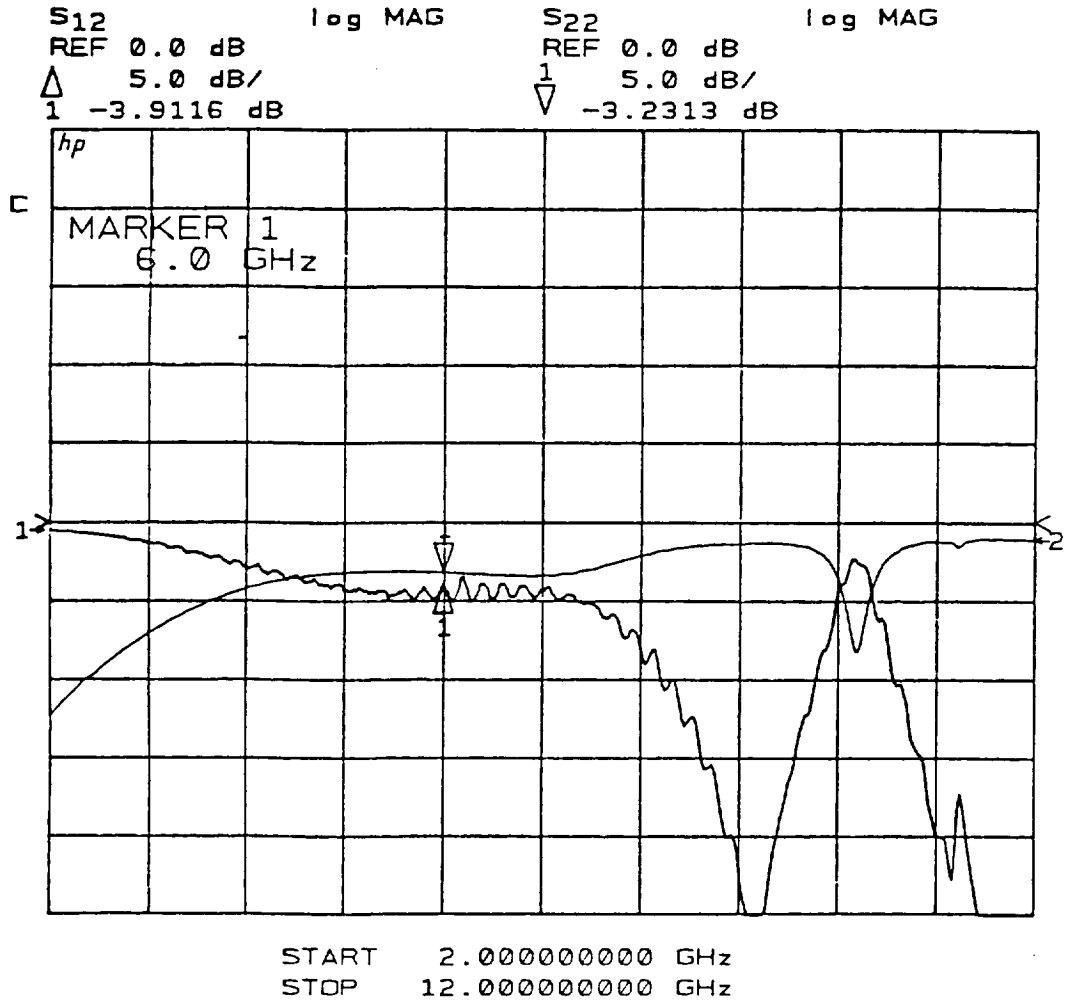

Figure 27: Return loss and insertion loss seen by the microstrip feedline of the prototype cavity-backed slot antenna.

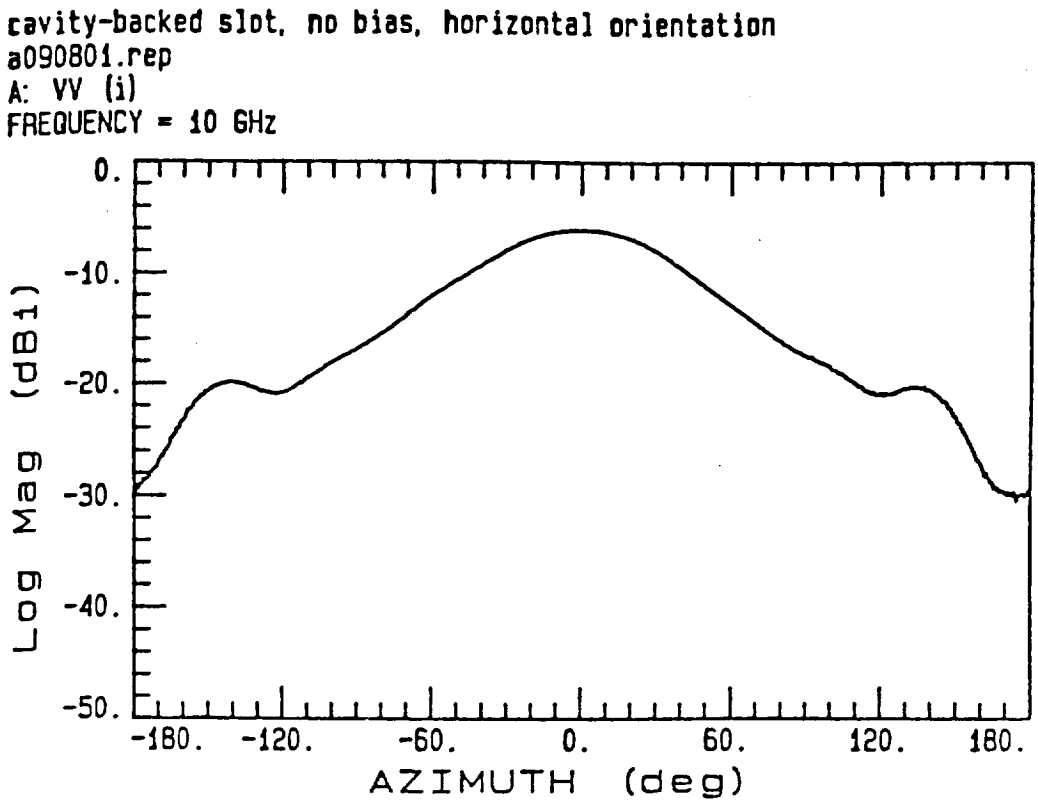

Figure 28: H-plane co-polarized radiation pattern of the prototype cavity-backed slot antenna.

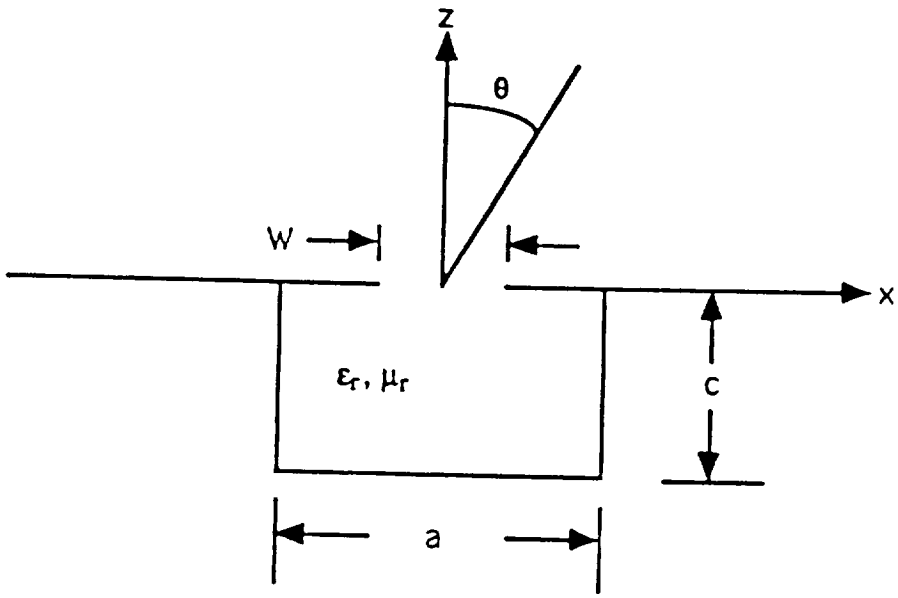

Figure 29: Geometry of a two-dimensional cavity-backed slot antenna.

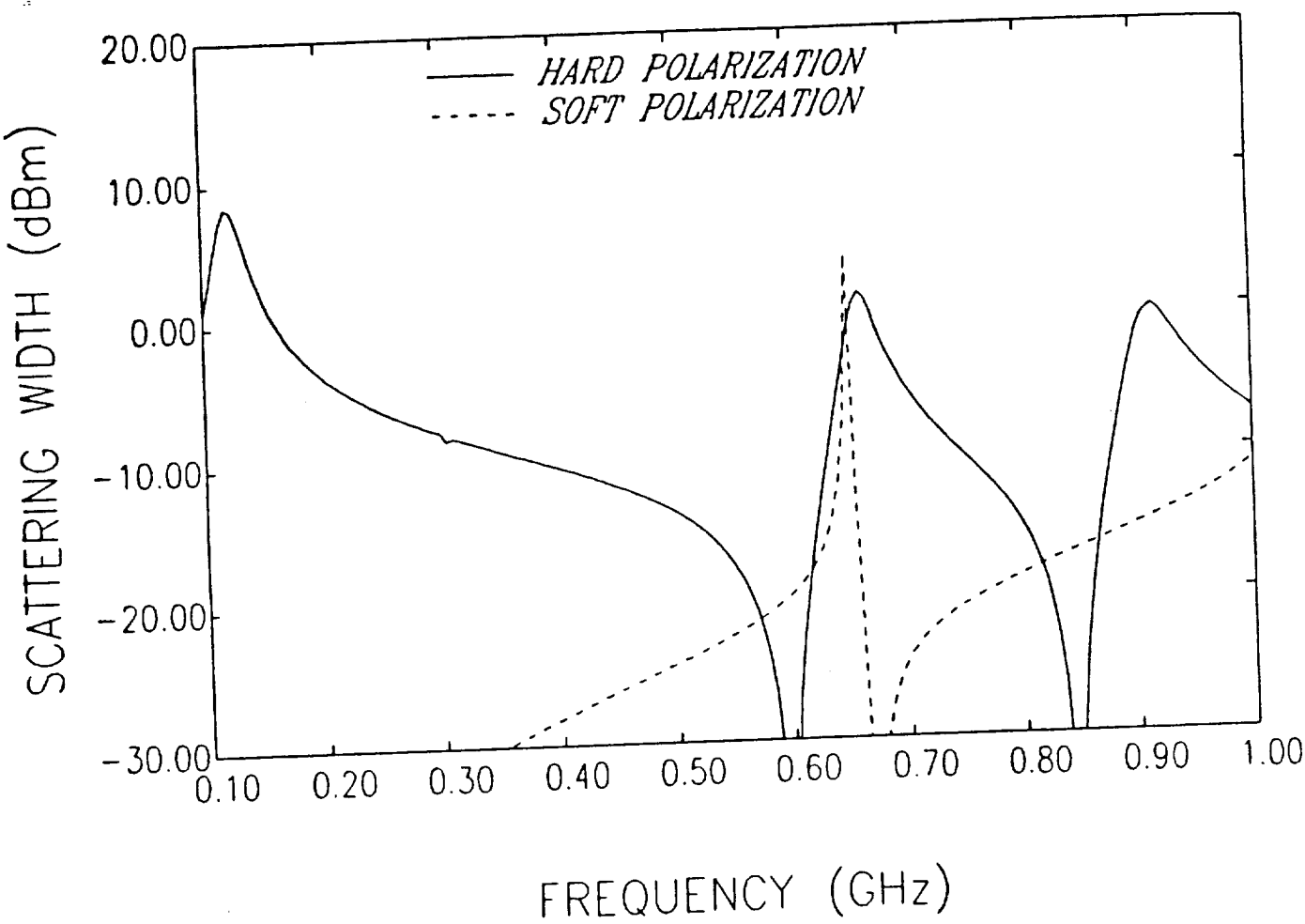

Figure 30: Monostatic scattering width of a two-dimensional cavity-backed slot antenna for hard and soft polarizations.

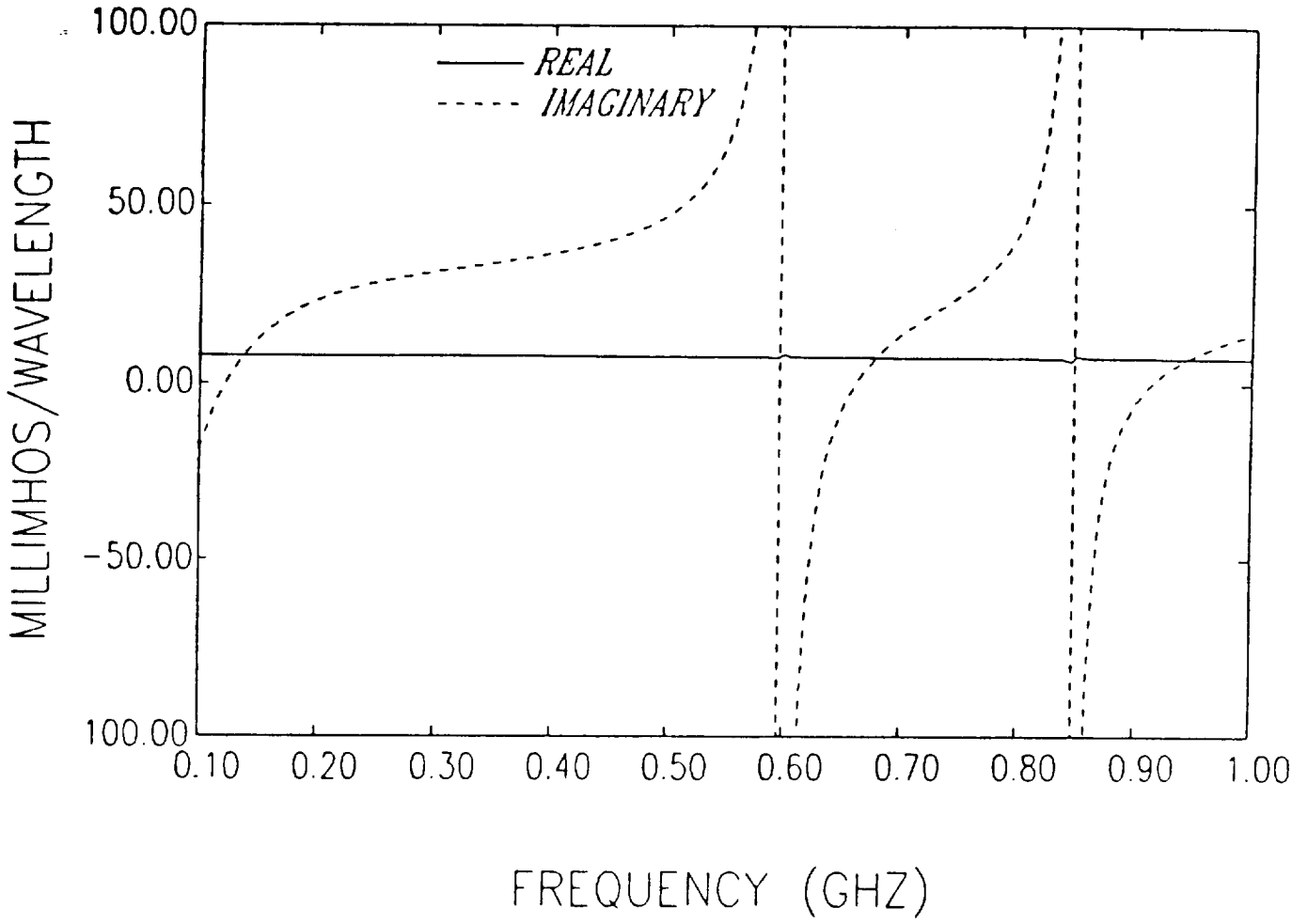

Figure 31: Input admittance of a two-dimensional cavity-backed slot antenna.

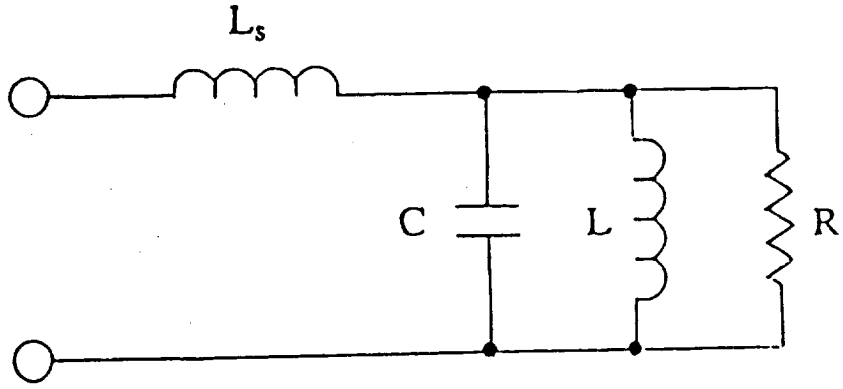

Figure 32: Equivalent circuit of a microstrip patch antenna based on the cavity model.

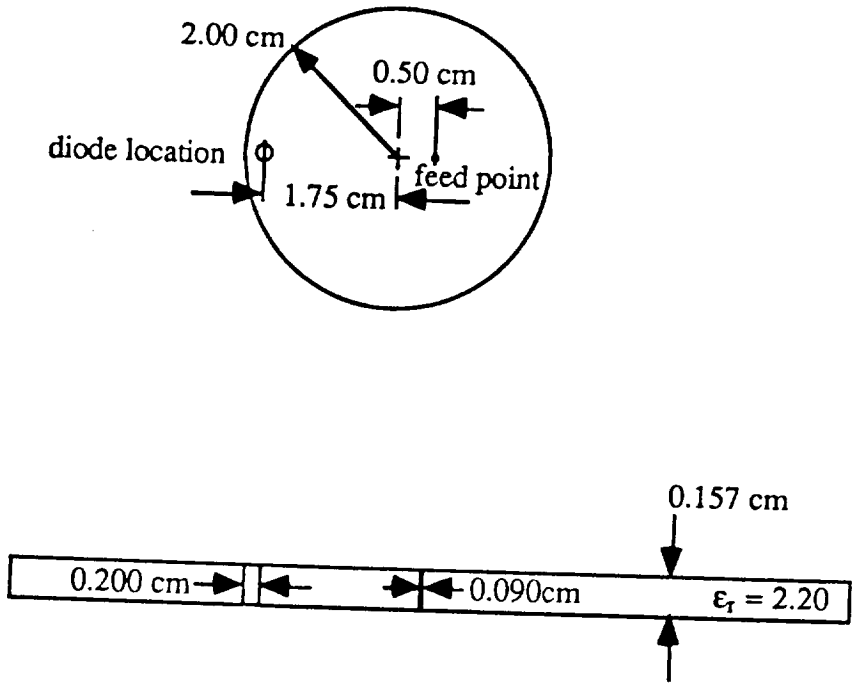

Figure 33: Geometry of the prototype varactor-tuned circular microstrip patch antenna.

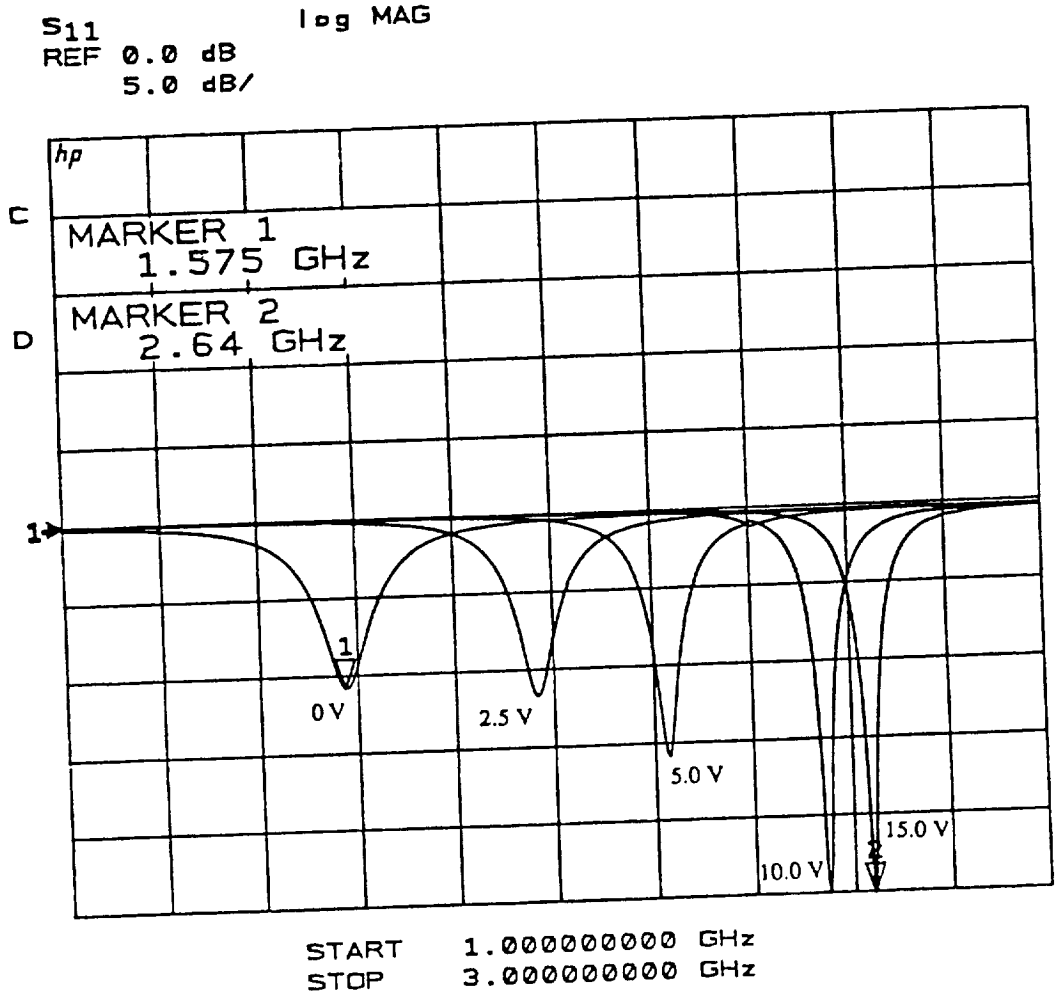

Figure 34: Measured input return loss of the prototype varactor-tuned circular microstrip patch antenna versus frequency for various bias voltages.

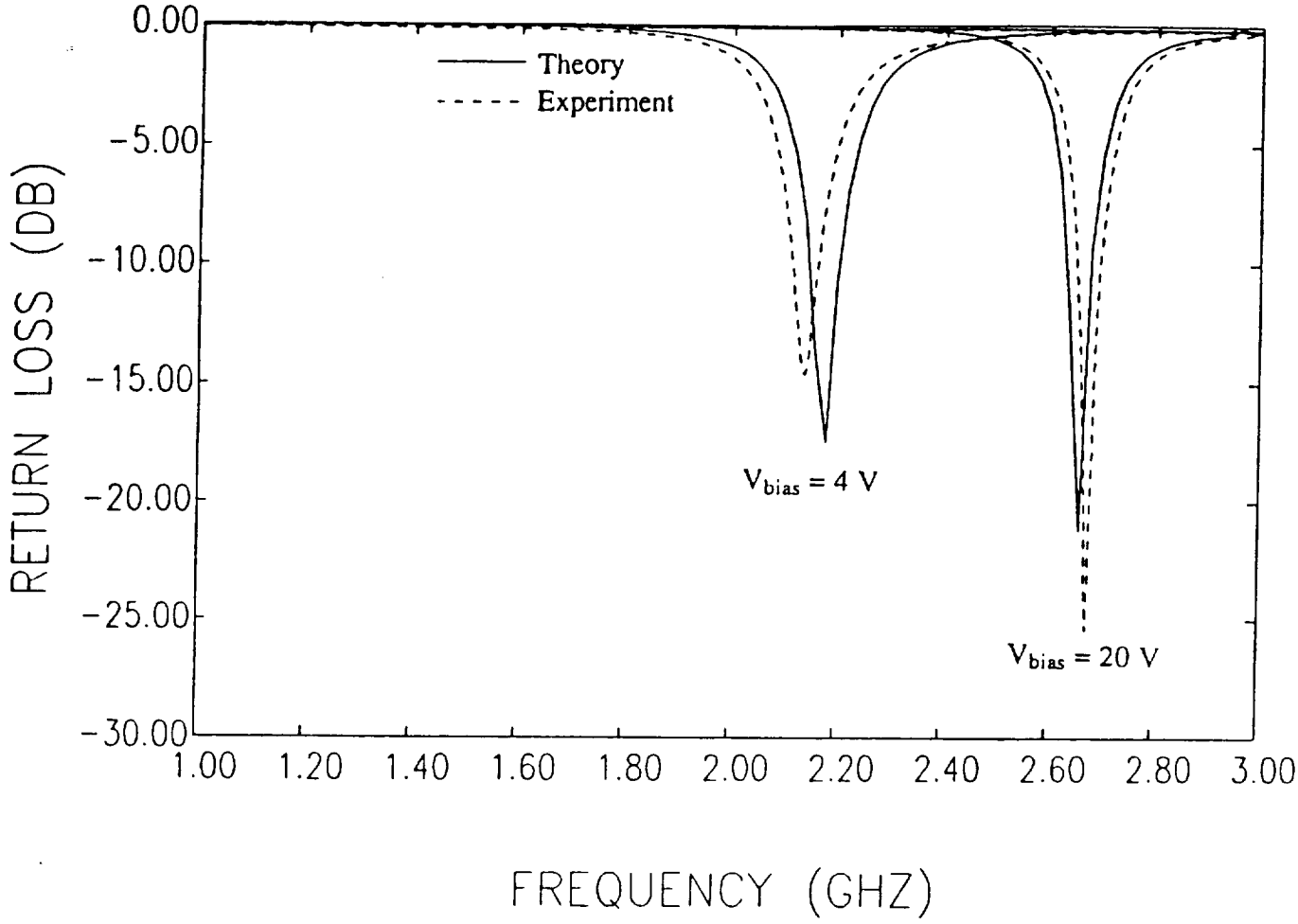

Figure 35: Measured and calculated input return loss of the prototype varactor-tuned circular microstrip patch antenna versus frequency for bias voltages of 4 and 20 volts.

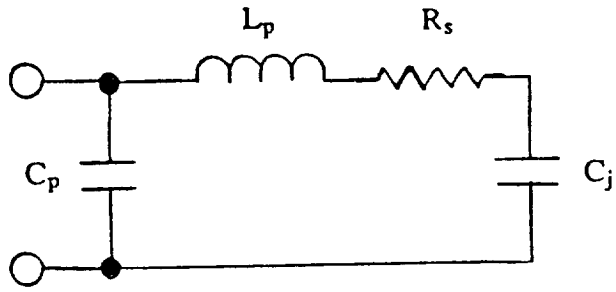

C_p = package capacitance = 0.15 pF

L_p = package inductance = 0.40 nH

R_s = series resistance = 2.27 Ω

C_j = junction capacitance = 2.402 pF @ V_{bias} = 4 V, 0.558 pF @ V_{bias} = 20 V

Figure 36: Equivalent circuit of the M/A-COM MA4ST556_31 varactor diode.

References

[1] W. A. Radasky, "An examination of adequacy of the three-species air chemistry treatment for the prediction of surface burst EMP," Mission Research Corporation, prepared for Defence Nuclear Agency, AD-A025 280, Dec. 1975.

[2] R.S. Elliott, "Antenna Theory and Design," Prentice-Hall, Inc., Englewood Cliffs, New Jersey 07632 1981, Ch 9, Sec. 4.

[3] C. A. Balanis, "Antenna Theory: Analysis and Design", John Wiley & Sons, Inc., pp. 733-734, 1982.